

Spectral and Polarization Vision: Spectro-polarimetric Real-world Dataset (Supplementary Information)

Yujin Jeon^{1,*} Eunsue Choi^{1,*} Youngchan Kim¹ Yunseong Moon¹
Khalid Omer² Felix Heide³ Seung-Hwan Baek¹
¹ POSTECH ² Meta ³ Princeton University

In this supplemental document, we provide additional analysis and details in support of the findings in the main manuscript.

Contents

1. Additional Comparison to Existing Datasets	2
2. Acquisition Setup	3
3. Spectro-polarimetric Image Formation	3
4. Noise and Denoising	4
5. Spatio-spectral-polarimetric Representation Methods	6
5.1. PCA	6
5.2. INR Network Architecture	6
5.3. Additional Results	6
6. Polarized and Unpolarized Intensity	9
7. Stokes-vector Distributions	12
8. Gradient Analysis	18
9. Shape from Polarization	20
10 Dataset Examples	22

*Equal contribution

1. Additional Comparison to Existing Datasets

We further highlight here the difference in dataset diversity between our datasets and prior works. The common datasets used in the field have been limited to polarization states, the number of spectral bands, scene count, and scene diversity, whereas our study expands the scope to include factors mentioned above.

Table 1 provides a comprehensive comparison between previous studies and our current research at a glance. In the "Polar." column, cells colored red indicate datasets encompassing only linear polarization states, whereas green cells denote datasets that include both linear and circular polarization states. Assessing the "# of bands" column, datasets providing grayscale polarization data are marked in red. Those offering spectral bands of 10 or fewer are colored yellow, while green cells indicate datasets that provide Stokes vectors for more than 10 spectra. In terms of scene count, works featuring 1 to 100 scenes are highlighted in red, those with 101 to 1000 scenes are in yellow, and green cells represent datasets with more than 1001 scenes. For scene diversity, datasets colored red consist of very limited scenes, such as synthetic scenes or objects in consistent conditions. Yellow cells represent limited scene types, like diverse objects or scenes within restricted environments, whereas green cells indicate natural scenes encompassing diverse environments.

Dataset	Polar.	# of bands	Scene count	Scene diversity
[10]	LP	1	522	Outdoor scenes
[1]	LP	1	300	Indoor objs.
[8]	LP	6	10	Indoor objs.
[14]	LP	3	40	Indoor objs.
[2]	LP	3	3	Indoor multiview
[2]	LP	3	2	Synthetic multiview
[4]	LP	3	6	Indoor multiview
[9]	LP	3	807	Reflective objs.
[11]	LP	3	500	Outdoor scenes
[6]	LP	3	44,300	Synthetic
[12]	LP	3	3,200	Reflective objs.
[13]	LP	3	4,500	Transparent objs.
[7]	LP	3	2,000	Indoor/outdoor scenes
[3]	LP, CP	18	67	Flat objs.
[5]	LP, CP	21	4	Synthetic multiview
[5]	LP, CP	21	4	Indoor/outdoor multiview
Ours (RGB)	LP, CP	3	2022	Indoor/outdoor scenes
Ours (hyperspectral)	LP, CP	21	311	Indoor/outdoor scenes

Table 1. Summary of relevant existing spectro-polarimetric image datasets.

- Lei et al. [10] (first row) offers grayscale linear polarization data confined to outdoor scenes.
- The work of [1] presents a dataset analogous to that of [10], both designed for shape-from-polarization (SfP) studies. The distinctive aspect of [1] is its focus on indoor objects, contrasting with the broader scene diversity of [10].
- [8] provides linear polarization data across 6 spectral bands, though with a limited range of captured objects.
- The study by [14] introduces a novel demosaicing technique for linear polarization data, showcasing a limited set of indoor object examples.
- [2] offers two varieties of linear polarization trichromatic data, including a few multiview datasets of indoor and synthetic scenes.
- [4] provides indoor scenes with vast number of views for trichromatic linear polarization state.
- [9] supplies linear polarization trichromatic data with a focus on reflected objects, encompassing a collection of under 1000 instances.
- [11] provides outdoor linear polarization trichromatic data, supplemented with NIR and LiDAR information.
- [6] produces synthetic linear polarization trichromatic data for the purpose of polarization scene rendering.
- Both [12] and [13] generate linear polarization trichromatic data with a considerable number of examples, though specifically limited to reflective and transparent scenes, respectively.
- [7] delivers a diverse indoor and outdoor scenes, but only in linear polarization across three wavelength channels.
- The work by [3] includes both linear and circular polarization states over 18 spectral bands. However, the dataset primarily

comprises flat objects captured in a laboratory environment, with the majority being refrigerator magnets, and the remainder consisting of 3D-printed and glued objects.

- [5] offers two types of datasets, each featuring linear and circular polarization data across 21 spectral channels. For each dataset type, they provide four examples: one comprising synthetic multiview data and the other containing multiview datasets of indoor and outdoor scenes.

Our dataset comprises two distinct types: one with extensive trichromatic Stokes data and the other with hyperspectral Stokes data encompassing 21 spectral bands, ranging from 450 nm to 650 nm at 10 nm increments. Both datasets provide linear and circular polarization information for a variety of indoor and outdoor natural scenes.

2. Acquisition Setup

To acquire full Stokes parameters, including both linear and circular polarization states, commercial polarization cameras typically require modifications, as they are originally designed to capture only linear polarization states. In the trichromatic Stokes imaging system developed by Tu et al. [16], as depicted in Figure 1(a) to (c), the foundational element is a standard polarization camera. This camera is fitted with a Bayer color filter array, over which four types of wire-grid linear polarizers are placed, corresponding to the color filters. This arrangement facilitates the capture of linear polarization characteristics. In addition, micro-retarders with a retardance of 45° and two distinct fast axes are alternately attached to the system. These micro-retarders behave like quarter wave plate (QWP) converting the incoming light into circularly polarized light. Consequently, for each pixel, the system captures 4×4 RAW intensities, equating to four polarized intensities for every set of four Bayer color filter pixels.

The hyperspectral Stokes imaging system designed by Kim et al. [5] utilizes monochromatic sensor to capture grayscale intensity of light from various spectral bands. The light sequentially passes through a QWP oriented at one of four distinct angles, $\theta \in \{30^\circ, -45^\circ, 60^\circ, -90^\circ\}$, during separate exposures. Subsequently, it traverses an LCTF, which functions as a linear polarizer and selectively capture light at desired wavelengths, before reaching the camera sensor.

3. Spectro-polarimetric Image Formation

After acquiring the RAW intensity data of a scene, several post-processing steps are undertaken to accurately reconstruct the Stokes parameters. For the trichromatic camera, the captured scene is initially in the form of RAW data with a resolution of 2048×2448 pixels. This data is subdivided into 16 distinct segments. The subdivision process involves categorizing each pixel based on its row and column indices (n, m) . Here, pixels are systematically assigned to specific segments using the formula $(n \bmod 4) \times 4 + (m \bmod 4)$, effectively distributing them across these segments. Each of these segments possesses a resolution of 512×612 pixels. We can see 16 segments in the right-most of Figure 1(b). Each partition is assigned to K -th segments, where $K = (n \bmod 4) \times 4 + (m \bmod 4)$.

We subsequently demosaic the 512×612 image into a 2048×2448 image, resulting in each spatial pixel of the 2048×2448 image having 16 intensity values. However, due to minor artifacts observed at the borders of the captured intensity, we crop the image to a resolution of 1900×2100 to ensure image quality. Subsequently, utilizing a pre-calibrated 16×12 reconstruction matrix, we derive four Stokes vectors for each of the three RGB components, total 12 values for each spatial pixel.

For the hyperspectral Stokes vector, we acquire 84 measurements with 21 wavelength and four QWP angles for 512×612 pixels. Using these captured images, we can reconstruct $\mathbf{s}(\lambda, p)$, the Stokes vector at a wavelength λ for a pixel p , by solving the least-square problem with $\mathbf{M}(\theta_k, \lambda, p)$, a per-pixel Mueller matrix of the entire system including a QWP oriented at θ_k :

$$\operatorname{argmin}_{\mathbf{s}(\lambda, p)} \sum_{k=1}^4 (I_{\text{meas}}^{\lambda, \theta_k}(p) - \mathbf{M}(\theta_k, \lambda, p; \lambda) \mathbf{s}(\lambda, p))^2, \quad (1)$$

where $I_{\text{meas}}^{\lambda, \theta_k}(p)$ is an intensity measurement for the pixel p at a wavelength λ with QWP of fast-axis angle θ_k .

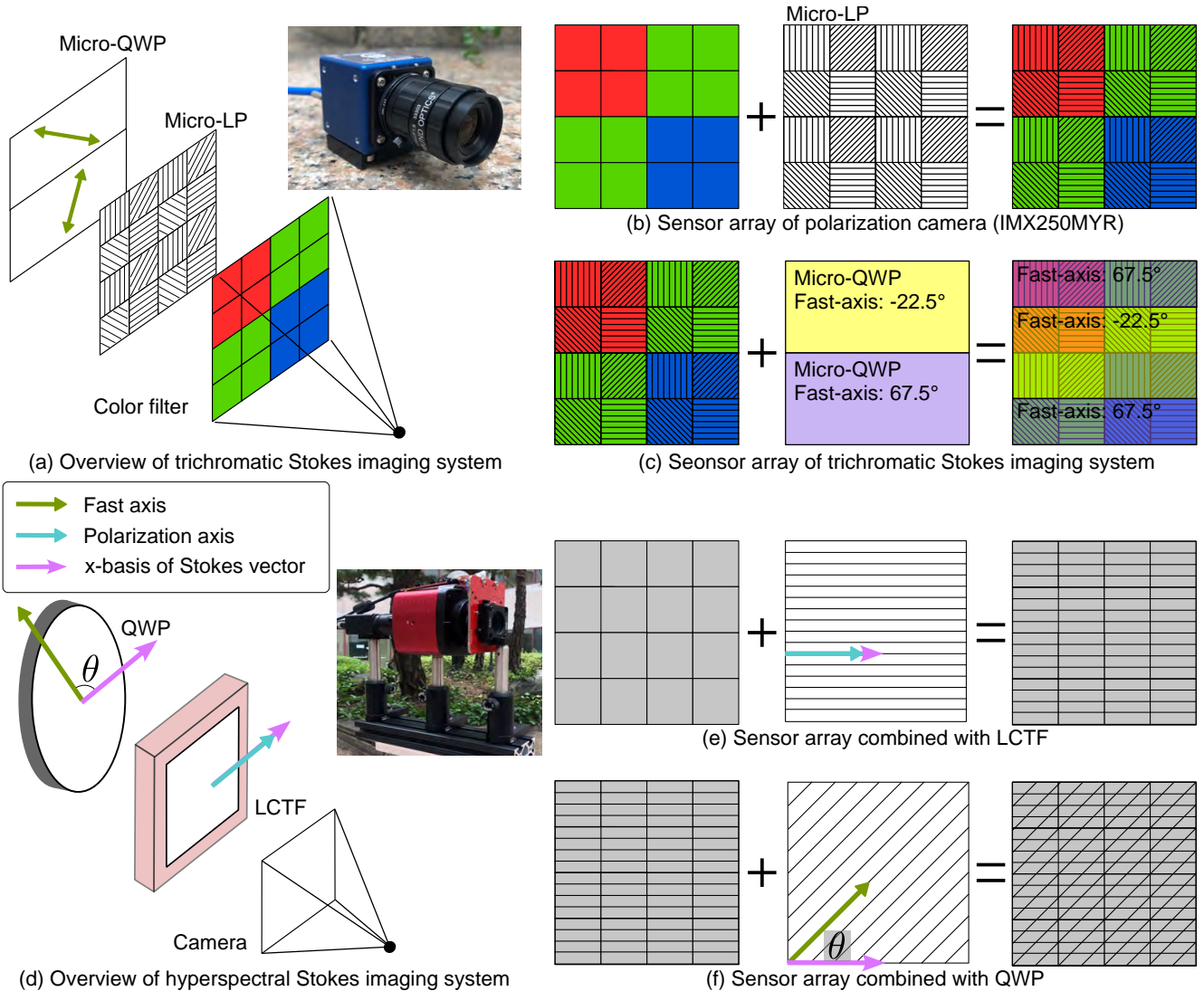


Figure 1. **Stokes Imaging Acquisition System.** (a) shows overview of acquisition system of trichromatic Stokes dataset. (b) illustrates structure of sensor array, SONY IMX250MYR, used widely in general polarization cameras. (c) represents the polarization sensor combined with micro-retarders which functions like quarter wave plate (QWP). (d) shows overview of hyperspectral Stokes imaging system. (e) and (f) illustrate sensor array of the hyperspectral system, equipped with LCTF and QWP.

4. Noise and Denoising

Images from the full-stokes camera can contain severe noise, especially for low intensity scenes. To suppress noise, we applied several approaches such as median filter and deep learning-based denoising network. We first employed a median filter to captured raw intensities, which is widely recognized for its efficacy in reducing noise while preserving edges in images. By moving through pixels in an image, it replaces with the median value of neighboring pixels. It reduces more noise compared to original data while losing details as the size of the median filter increases, as shown in Figure 2.

Similarly, we applied the state-of-the-art single-shot denoising method, KBNNet [17], on the captured RAW intensities. The outcomes, including the visualized polarization characteristics, are illustrated in the last column of the Figure 2. Comparing to the median filters, KBNNet preserves internal details while suppressing severe noise.

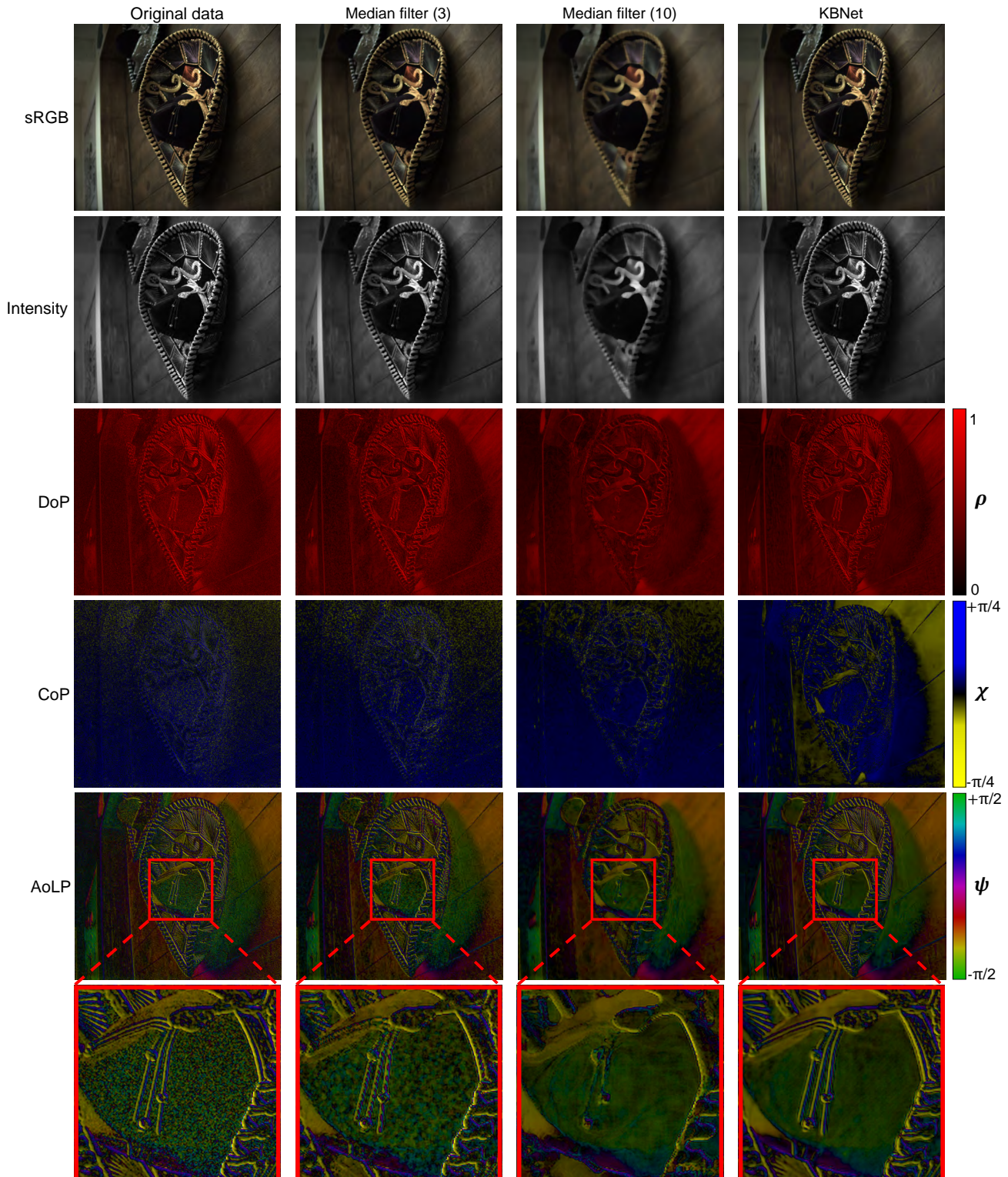


Figure 2. **Polarization Features of Denoised Stokes Vectors.** The first column shows noisy input data. The second and the third column represent results after applying median filter of size 3×3 and 10×10 respectively. The last column illustrates result after employing single-shot denoising method KBNNet [17]. Each row presents the polarization characteristics of the red channel from a trichromatic Stokes image, encompassing sRGB, intensity, DoP, CoP, and AoLP. The last row emphasizes a severely noisy portion of AoLP visualization of the original Stokes vector and that of denoised Stokes vectors.

5. Spatio-spectral-polarimetric Representation Methods

5.1. PCA

We conducted principal component analysis (PCA) on both trichromatic and hyperspectral Stokes dataset. We first divided the images into patches of size $P \times P$ patches, $P = 10$ in this time, resulting in 190×210 patches for one trichromatic Stokes image and 51×61 patches for one hyperspectral Stokes image, to efficiently extract a spatial basis.

After splitting, we flatten the patches and transform into 200 coefficients. We then derive the basis vectors for these Stokes patches:

$$\mathbf{p} = \mathbf{c} \cdot \mathbf{b} + \mu, \quad (2)$$

with \mathbf{b} as the basis, \mathbf{c} the corresponding coefficient, and μ the mean of incoming data. To store 10×10 size of Stokes parameters, we need $10 \times 10 \times t \times l$ parameters, where t denotes the number of Stokes parameters for one pixel, four, and l represents the number of spectral channels, which is 21 for the hyperspectral Stokes dataset and 3 for the trichromatic Stokes dataset. However, to represent with coefficients and bases, we need only 93 parameters for coefficients and one additional parameter for μ to achieve bits-per-pixel (BPP) 60 with reasonable results. Figure 4 illustrates the obtained bases of hyperspectral dataset. Each row matches the wavelength across spectral axis, and we can see that bases for each wavelength exhibit similar spatial characteristics with variations in scale.

5.2. INR Network Architecture

We modify the NeSpoF [5] to efficiently represent spectro-polarimetric information of a particular scene. We model the per-pixel MLP (F_{Θ}^p) and spectral MLP (F_{Θ}^c) without using intermediate polarimetric features, s_0 , DoP, χ , ψ , as shown in Figure 3. The per-pixel MLP extracts the per-pixel polarimetric feature f^p and the spectral MLP outputs the Stokes vectors from the per-pixel feature f^p and spectral channel c . We set the hyperparameter k of positional encoding [15] to 10 and 1 for the pixel coordinate (p_x, p_y) and spectral channel c , respectively:

$$\gamma_k(x) = [x, \sin(\omega_0 x), \cos(\omega_0 x), \dots, \sin(\omega_k x), \cos(\omega_k x)], \quad (3)$$

where $\omega_k = 2^k \pi$. To achieve BPP 60, we set the number of layers 8, which consumes 2.22 MB to store 100 MB Stokes data.

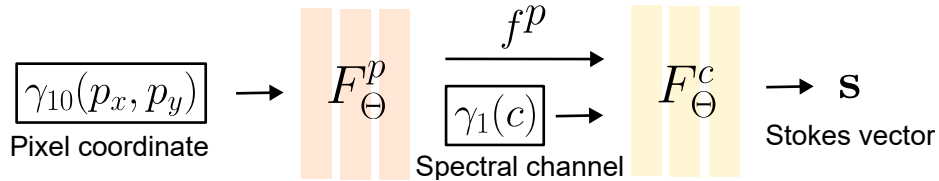


Figure 3. Network architecture.

5.3. Additional Results

Above, we show that employing PCA and INR can reduce the memory footprint of data. Consequently, this approach also facilitates effective denoising of the data. As shown in Figure 4(d) and (f) of the main text, a comparison with pseudo ground-truth(pseudo-GT) Stokes vectors, generated through burst imaging of a hundred images, reveals that the PCA method yields a mean squared error (MSE) of 2.69×10^{-5} , while the INR approach exhibits an MSE of 1.90×10^{-5} . Figure 5 presents visualizations of various polarization characteristics and the components s_1 , s_2 , and s_3 of the Stokes vectors of the original scene. It also showcases the outcomes produced by PCA, NeSpoF, the denoising method, and burst imaging. The denoised Stokes vectors exhibit the lowest error, however, unlike PCA and INR, they do not facilitate data size compaction.

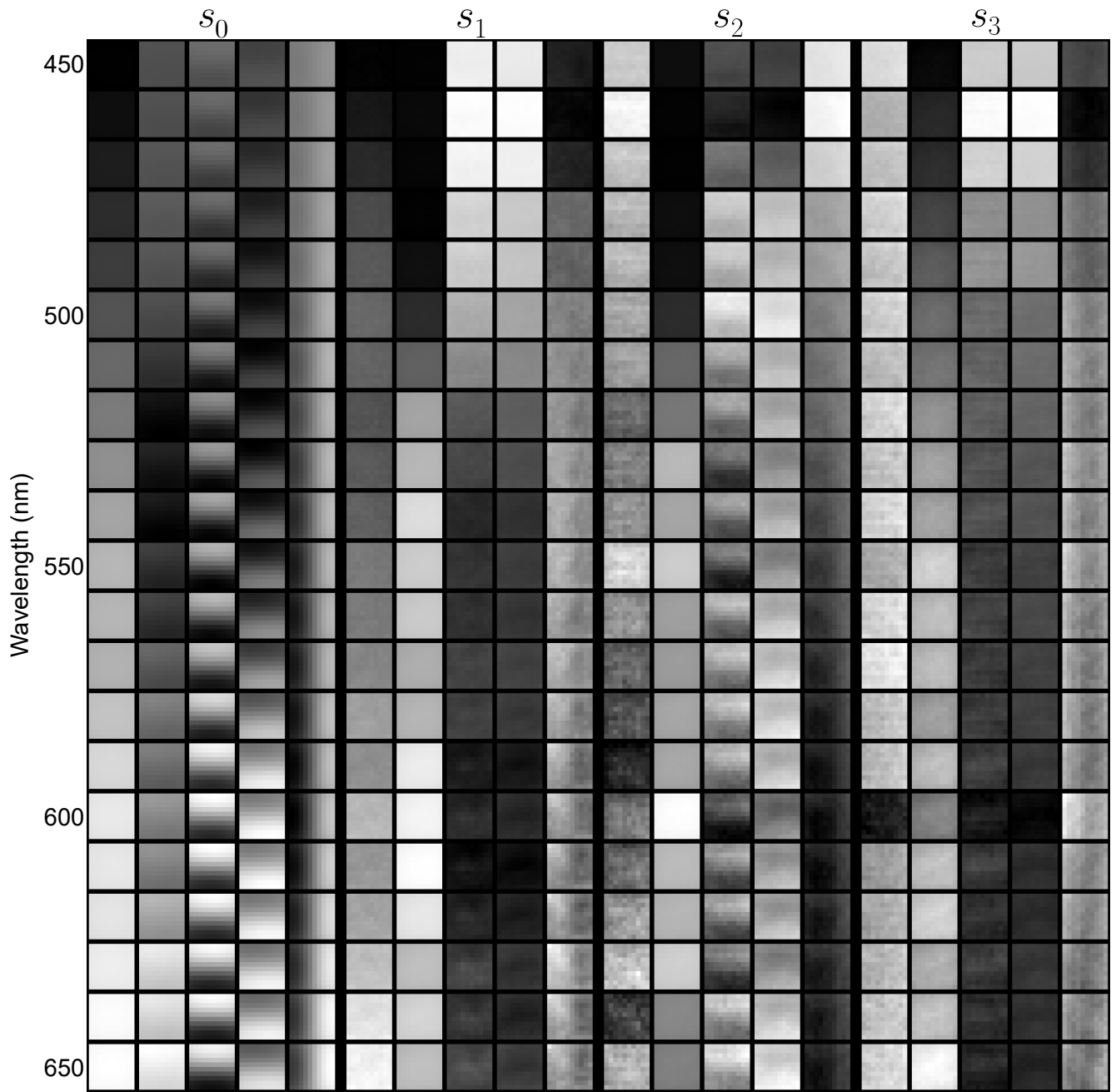


Figure 4. **Bases obtained via PCA.** each row corresponds to a specific wavelength along the spectrum axis starting from 450 nm and increasing in increments of 10 nm, culminating at 650 nm. The columns are broadly categorized into s_0 to s_3 , and within each group, there are five columns that represent five most significant bases.

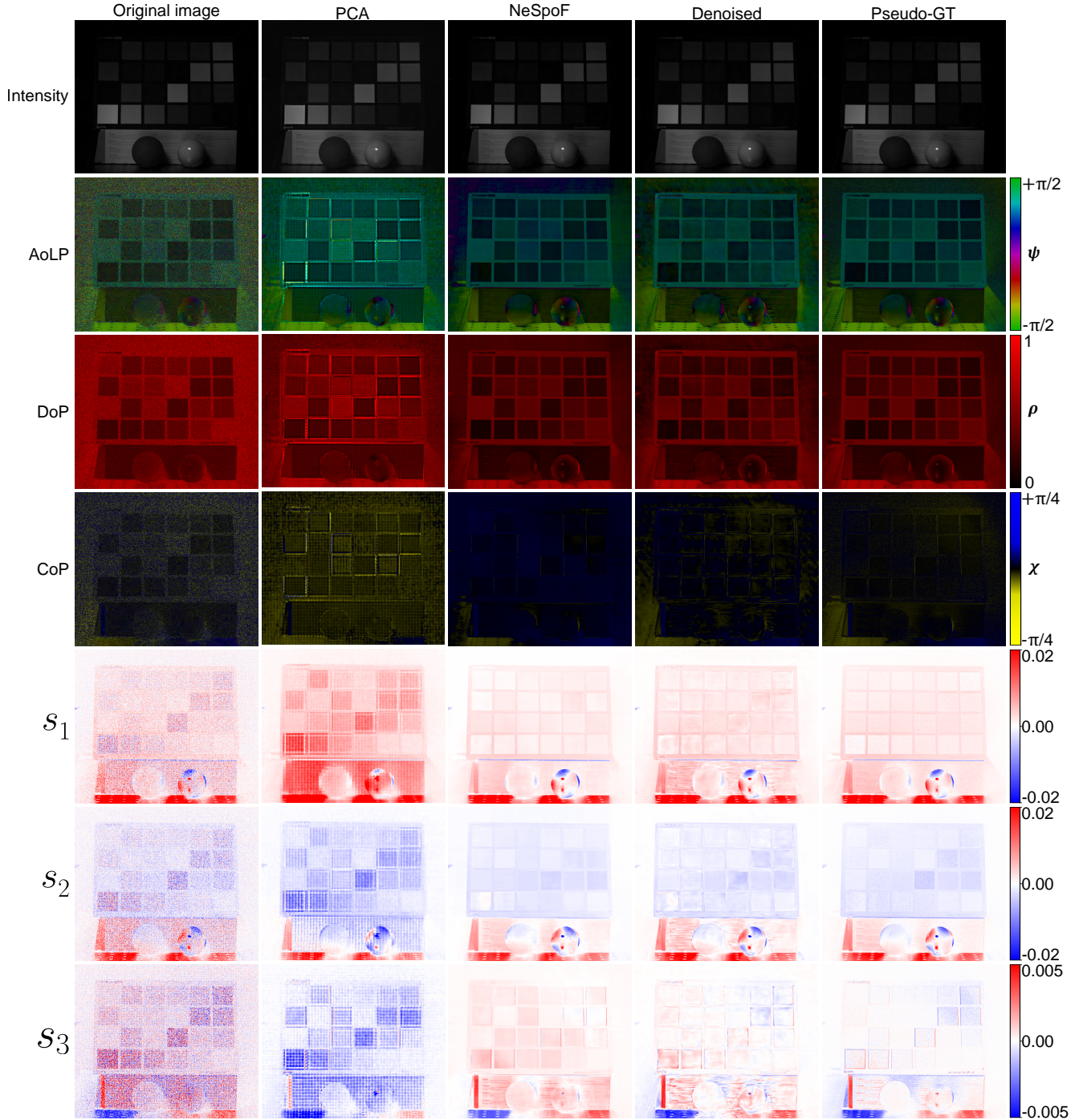


Figure 5. **Results after Compressive Polarization Representation.** Each column shows original Stokes image, Stokes vectors reconstructed from bases and coefficients by PCA, results after NeSpoF, Stokes vectors reconstructed from denoising methods by [17] and pseudo ground truth Stokes parameters obtained by burst-imaging 100 images. Each row illustrates Stokes vectors and polarization characteristics of 550 nm, encompassing sRGB, intensity and AoLP, DoP, CoP visualization, and s_1 , s_2 , s_3 information.

6. Polarized and Unpolarized Intensity

This section presents additional results from the decomposition of our datasets into polarized and unpolarized light. Figure 7 shows the separated polarized and unpolarized images of 18 different scenes in our trichromatic dataset, while Figure 8(a), (b) and (c) shows the same results across the spectrum for one scene in our hyperspectral dataset. As discussed in the main paper, it is evident from our observations that polarized images contain specular reflections, such as the glow of glass. Notably, outdoor scenes captured under sunlight exhibit a rainbow-colored polarization of the sky. Additionally, we can confirm that the LCD display on a monitor mainly emits polarized light, as shown in Figure 7.

Furthermore, we conducted an analysis of the intensity distributions for polarized and unpolarized components concerning the dataset labels. Figure 6 shows that, irrespective of the label, the intensity of polarized light skews towards low and high-intensity values compared to unpolarized light. However, distinct patterns emerge when comparing intensity distributions captured under sunlight and cloudy conditions. In the cloudy dataset, polarized light is more concentrated near zero compared to the sunlight dataset, and a peak is observed in the middle of the graph. As polarized sunlight passes through clouds, it undergoes scattering events, leading to changes in its polarization states. The distinct polarization properties arising from varying illumination conditions will be further discussed in the subsequent analysis sections.

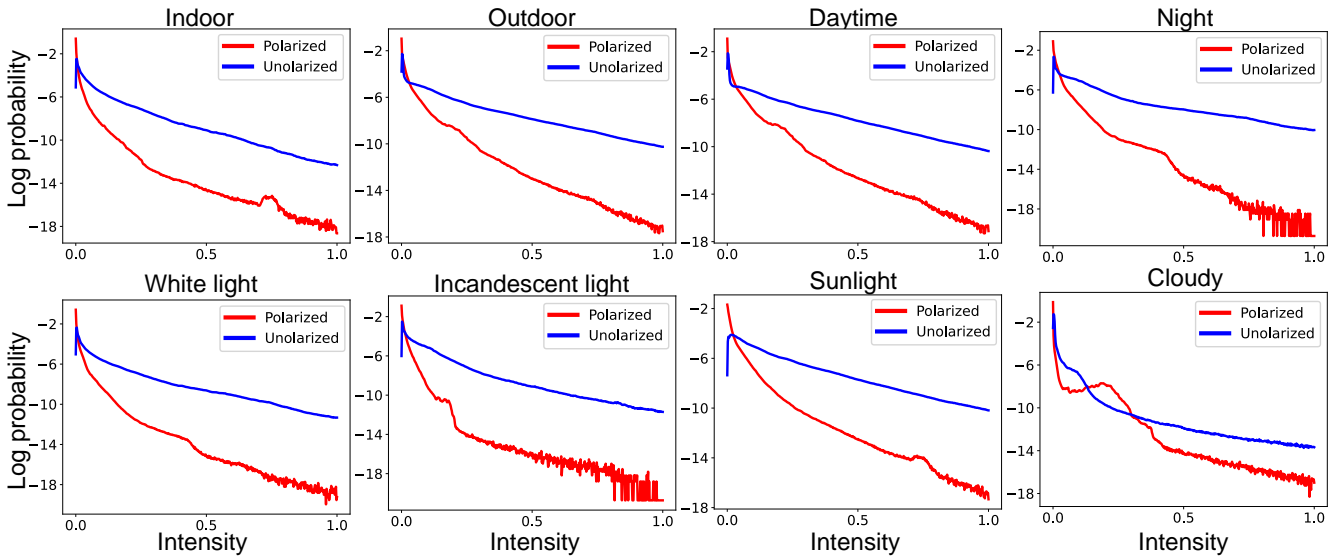
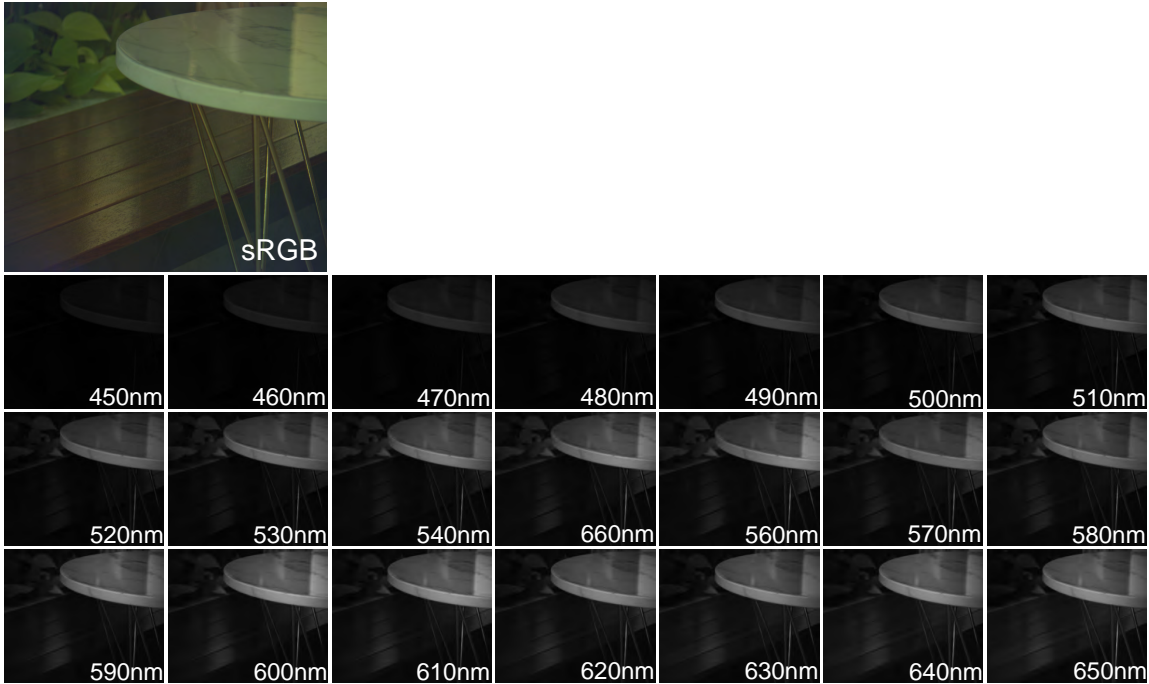


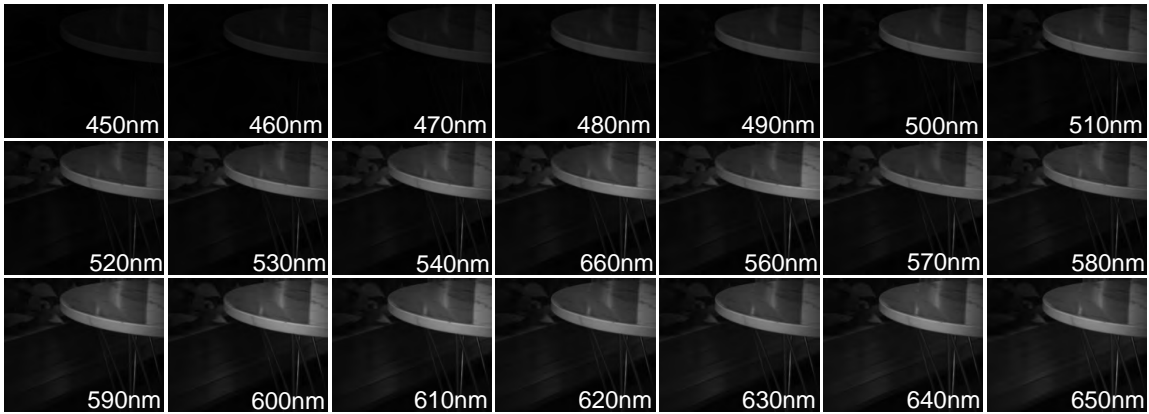
Figure 6. Intensity distributions for polarized and unpolarized components with respect to dataset labels.



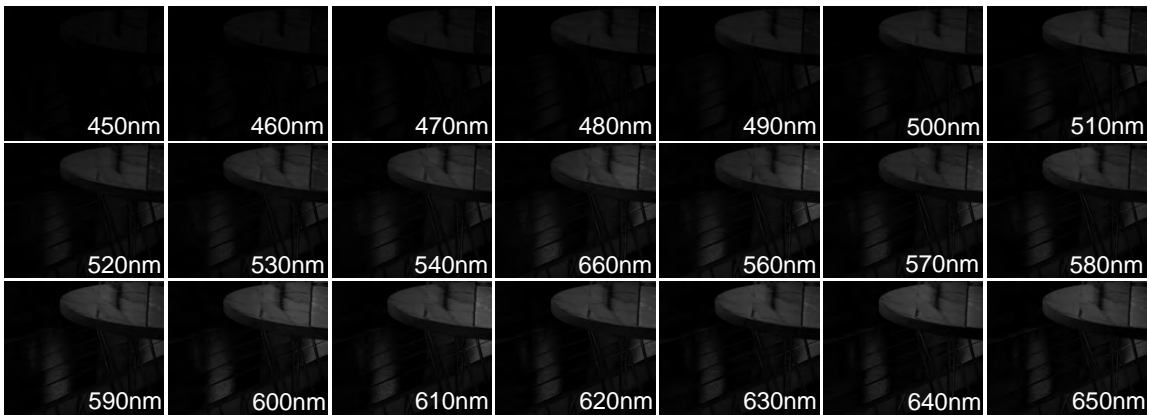
Figure 7. Additional results of separation into polarized and unpolarized light in the Trichromatic dataset.



(a) Intensity with respect to spectrum



(b) Unpolarized light with respect to spectrum



(c) Polarized light with respect to spectrum

Figure 8. **Additional results of separation into polarized and unpolarized light in Hyperspectral dataset** Intensities and unpolarized lights are in range 0 to 1, and polarized lights are plotted in range 0 to 0.3 for visualization.

7. Stokes-vector Distributions

We analyze the distributions of Stokes-vectors concerning the spectrum and various capture environments based on our dataset labels.

Figure 9 highlights the diversity of the Stokes vectors across the spectrum. It visualizes the Stokes vector components s_1 , s_2 and s_3 for a scene in the hyperspectral dataset. As shown in Figure 8, the values of s_1 , s_2 and s_3 on the surface of the cone shows distinct distributions for each wavelength. Particularly, noteworthy is the significant difference in s_2 and s_3 values at 610nm and 620nm, despite only a 10nm separation. The hyperspectral polarization dataset proves instrumental in providing detailed insights into the analysis and decomposition of polarization information, in contrast to trichromatic polarization data.

Figure 10 highlights the impact of the capture environment on polarization states. The upper two scenes were captured outdoors, and the bottom scene was captured indoors. As shown in Figure 10, the intensity of Stokes vectors in outdoor scenes tends to be higher than in indoor scenes. Moreover, the outdoor scene captured under sunlight, which includes more circularly polarized light, exhibits greater variability in s_3 values compared to s_1 and s_2 across the R, G, and B channels. Conversely, for the indoor scene, s_1 and s_2 are widely distributed across color channels rather than s_3 .

Moreover, we conduct an analysis based on the dataset labels by plotting the distributions of Stokes vectors in both the hyperspectral and trichromatic datasets (Figure 11, 12). We observe that the components of the Stokes vector in the cloudy scene are concentrated near zero compared to the sunlight scene. This observation aligns with the understanding that polarized sunlight undergoes depolarization due to scattering events on the cloud, a phenomenon further illustrated in the Poincaré sphere visualization presented in the main paper. For the night scene, characterized by predominantly low-intensity pixels, Stokes vectors are distributed unstably and lack a symmetrical shape. Furthermore, the maximum number of pixels is significantly lower than that in the other scenes, indicating a dispersion of these values. Although the data captured under white light and incandescent light exhibit similar patterns in Stokes vector distributions, the maximum number of pixels in the incandescent light scene is lower than that in the white light scene. This indicates that scenes under the white light have a higher slope in its Stokes vector distributions compared to scenes under the incandescent light. This observation is further supported by the Poincaré sphere visualization (see Figure 13).

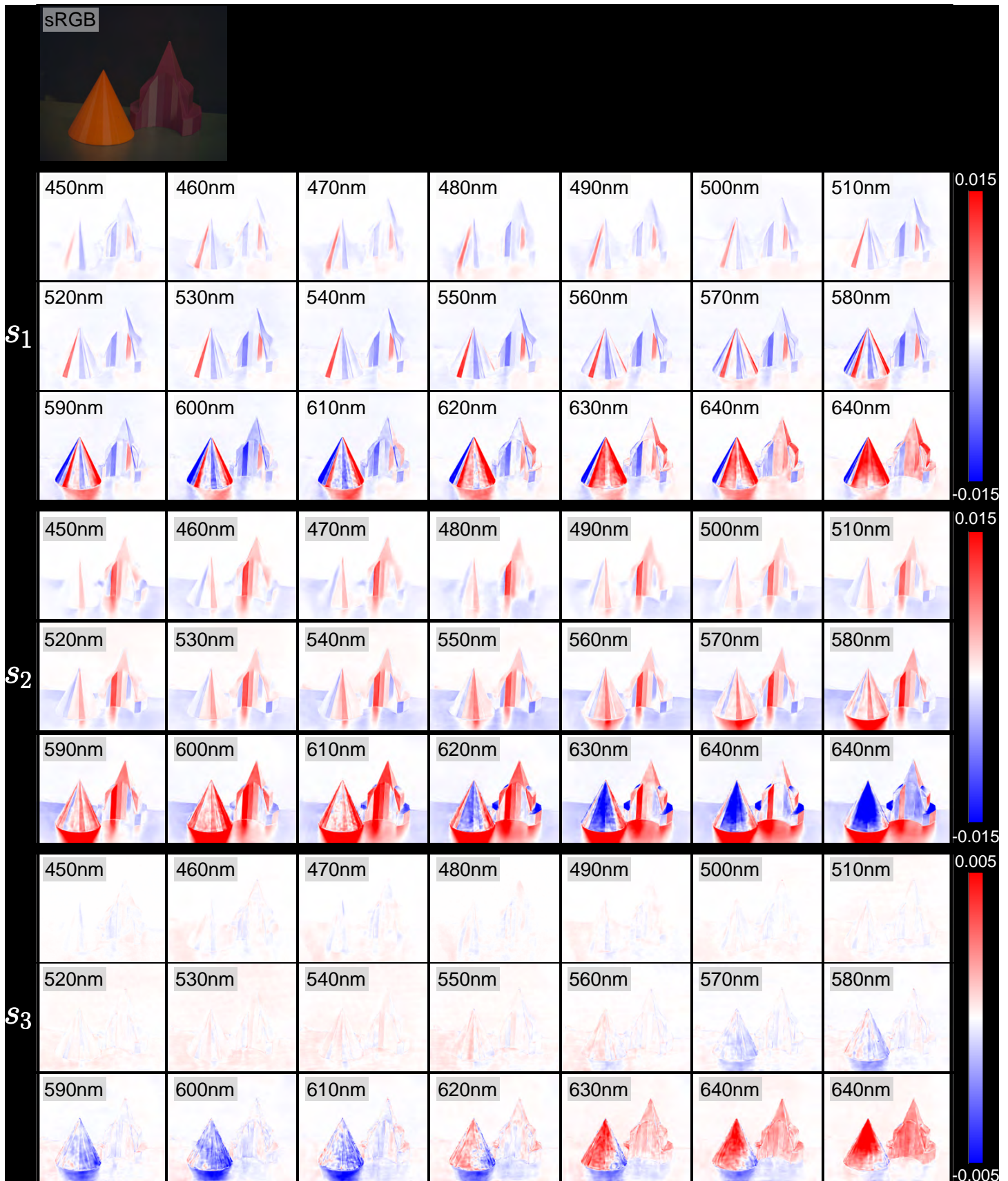


Figure 9. Stokes Images over the Spectrum. Stokes images of s_1 , s_2 and s_3 of hyperspectral dataset

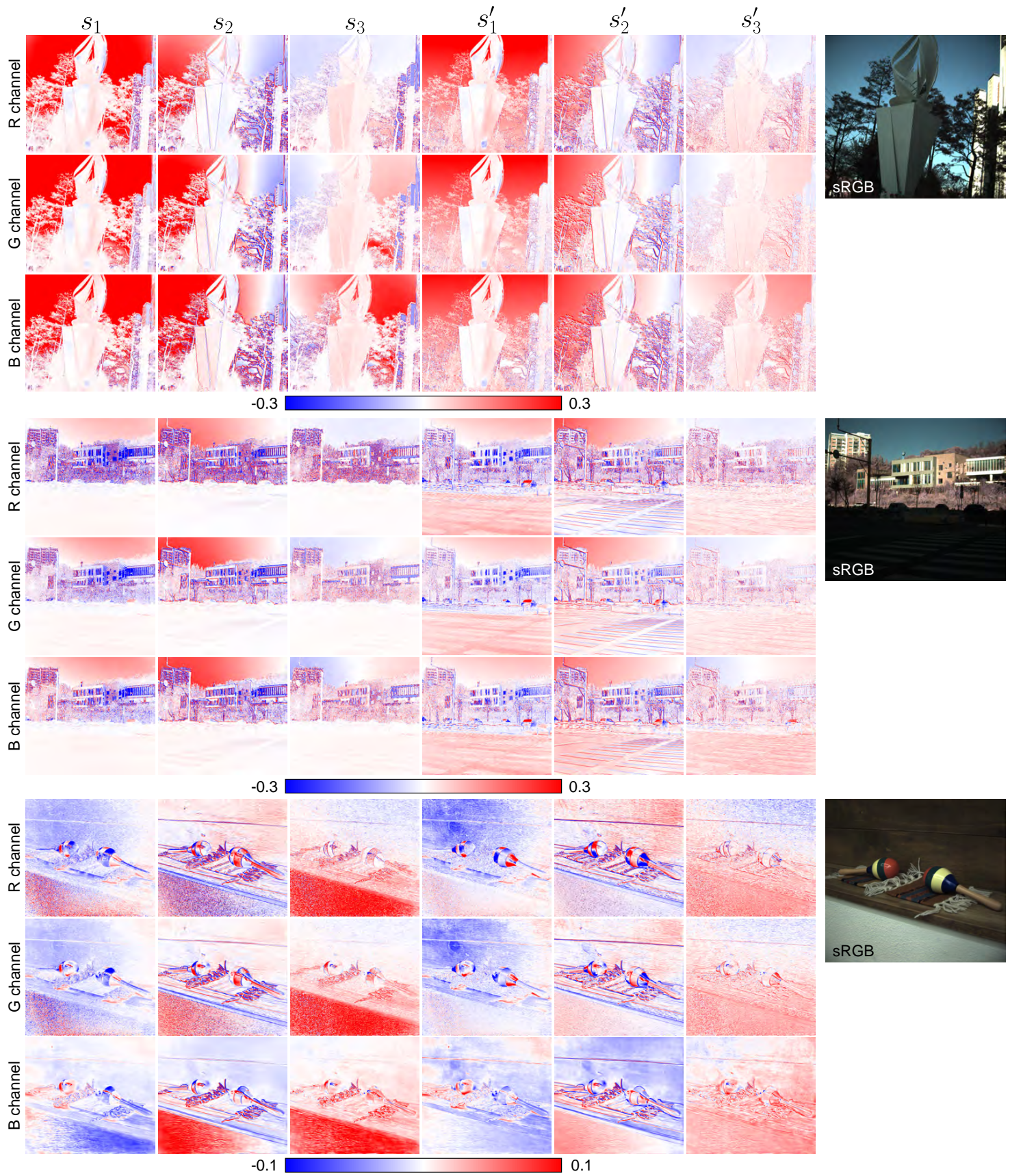
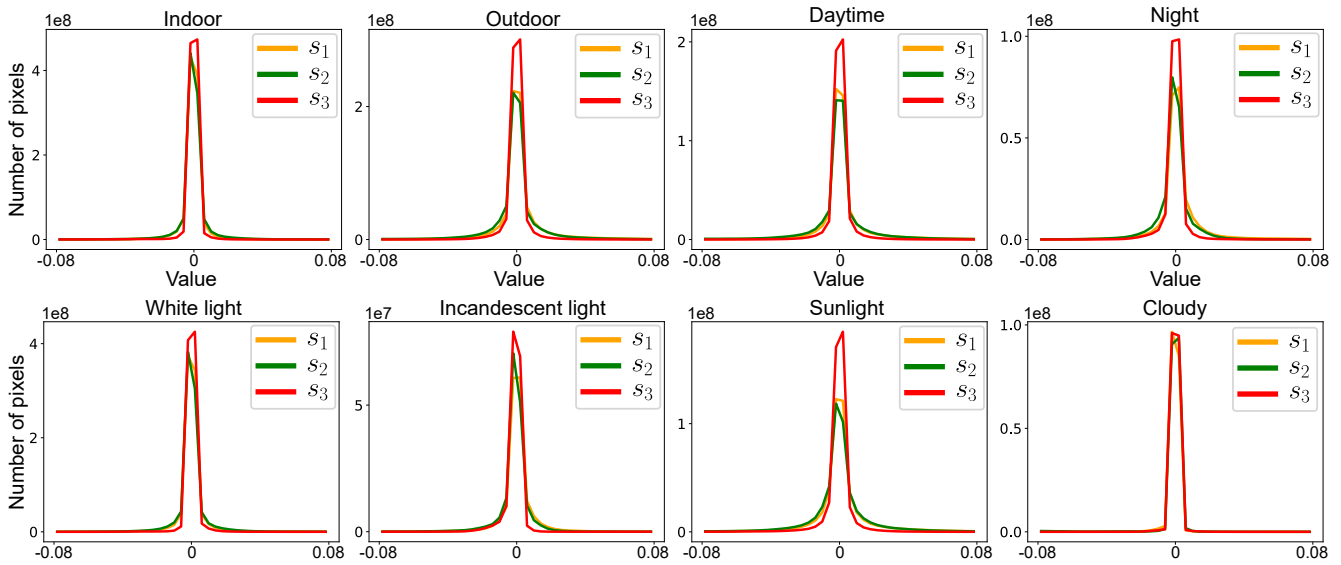
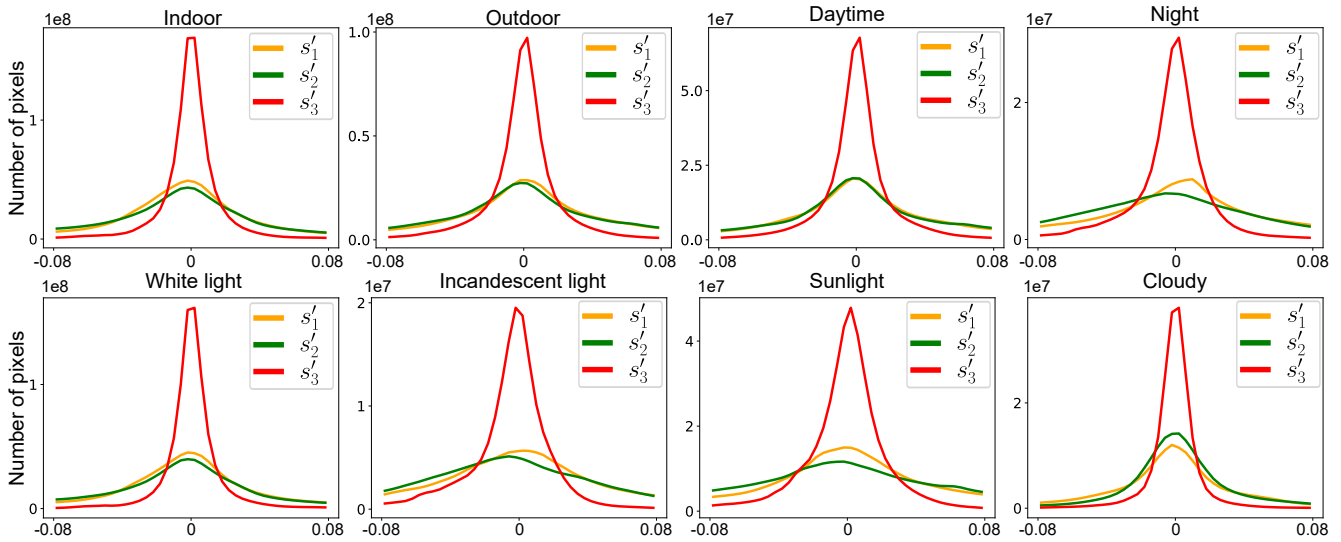


Figure 10. Stokes images at R, G and B channels. Stokes images of s_1, s_2 and s_3 of trichromatic dataset

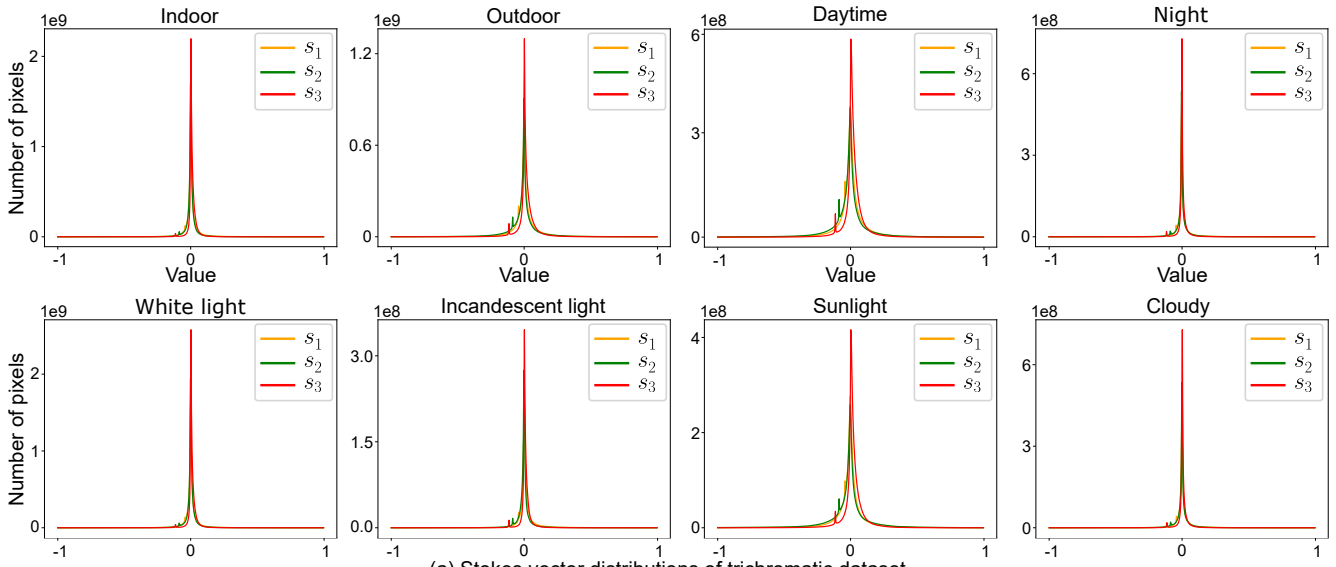


(a) Stokes vector distributions of hyperspectral dataset

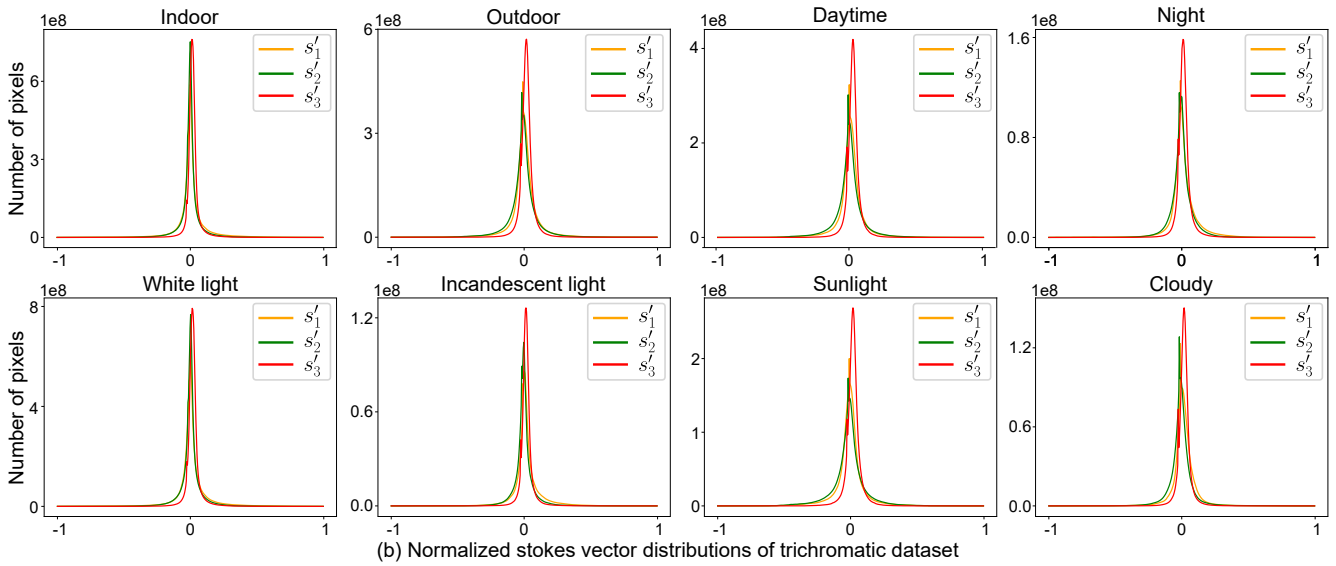


(b) Normalized Stokes vector distributions of hyperspectral dataset

Figure 11. Stokes-vector and normalized Stokes-vector distributions of hyperspectral dataset



(a) Stokes vector distributions of trichromatic dataset



(b) Normalized Stokes vector distributions of trichromatic dataset

Figure 12. Stokes-vector and normalized Stokes-vector distributions of trichromatic dataset

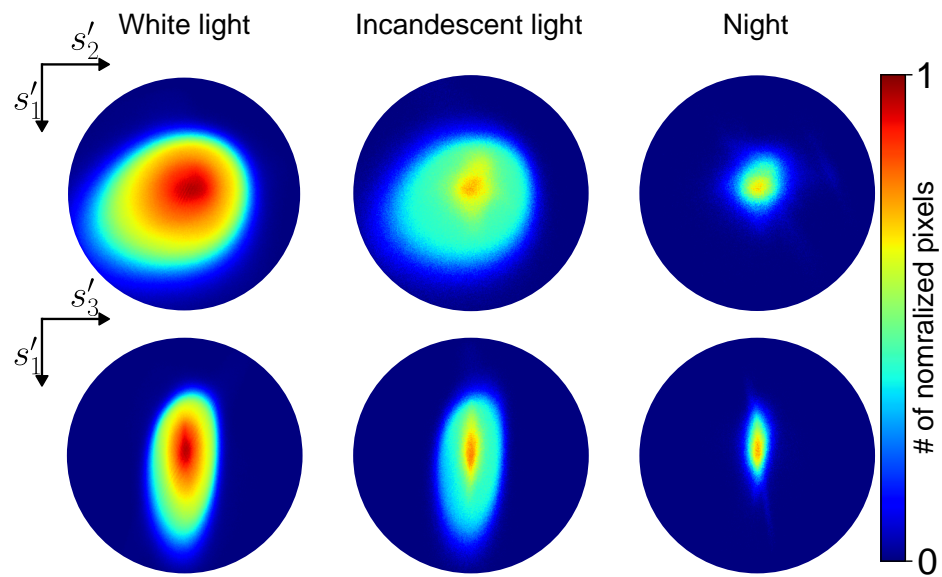


Figure 13. Poincaré sphere of white light, incandescent light and night scene

8. Gradient Analysis

In this section, we present additional gradient distributions based on the location and time of data capture (indoor, daytime, and night). As shown in Figure 14, we plot the gradient distributions of Stokes vectors (s_0 , s_1 , s_2 , and s_3), normalized Stokes vectors (s'_1 , s'_2 , and s'_3), Angle of Linear Polarization (AoLP), Chirality of Polarization (CoP), Degree of Circular Polarization (DoCP), and Degree of Linear Polarization (DoLP). Scenes captured at different locations and times exhibit distinct patterns in their gradient distributions, while still retaining similar shapes to the hyper-Laplacian prior. Interestingly, data captured during the daytime shows that the gradient of Stokes vectors (s_0 , s_1 , s_2 , and s_3) is distributed more widely compared to indoor and night scenes. However, for the normalized Stokes vectors s'_1 , s'_2 , and s'_3 , daytime scenes are more concentrated near zero than others.

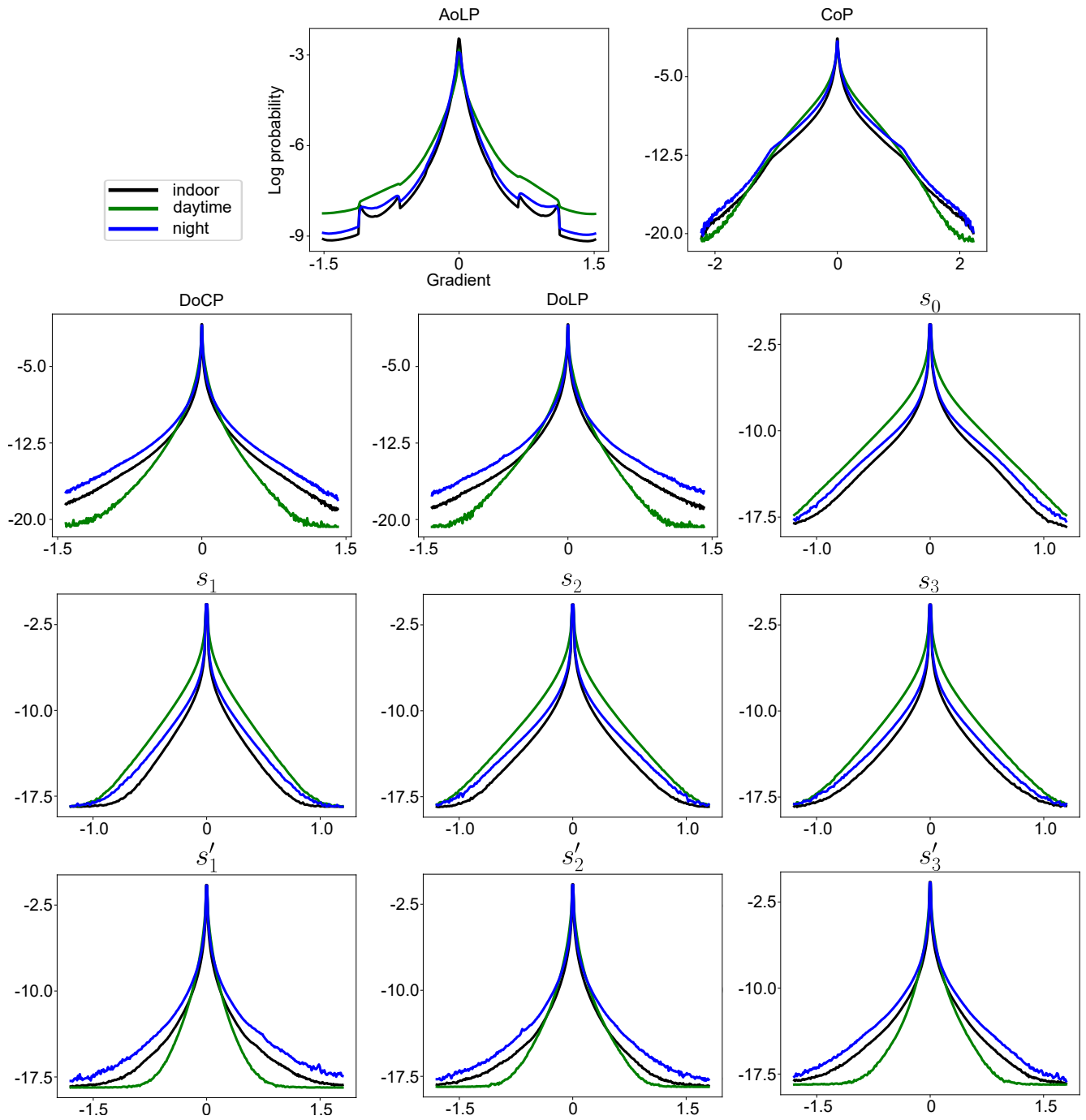
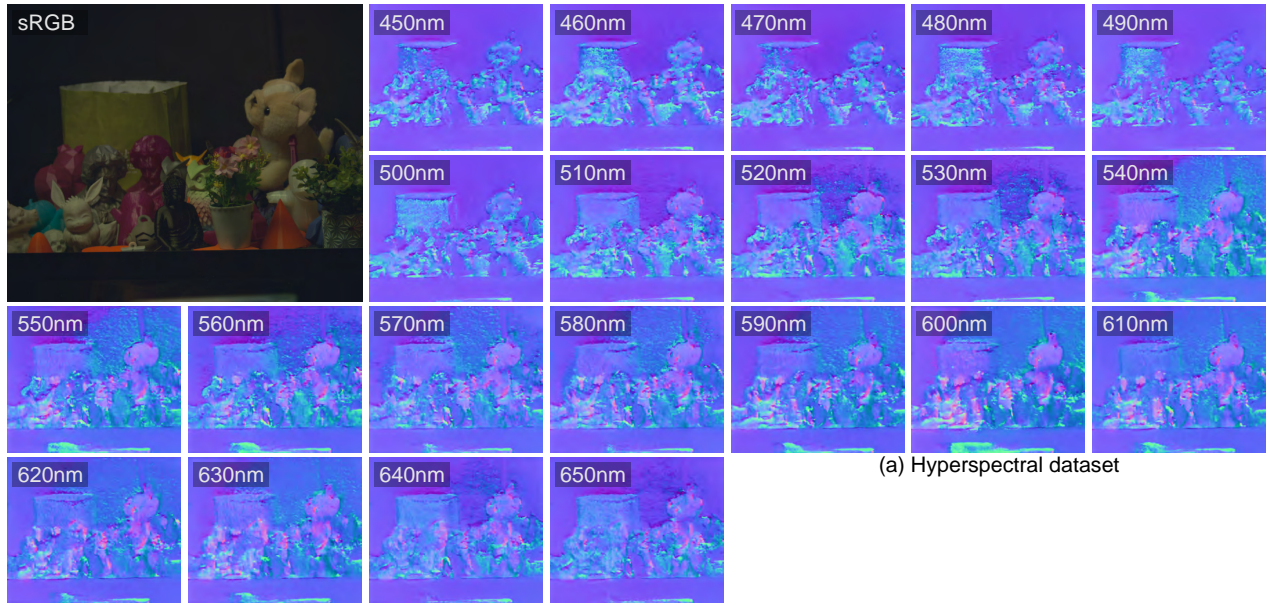


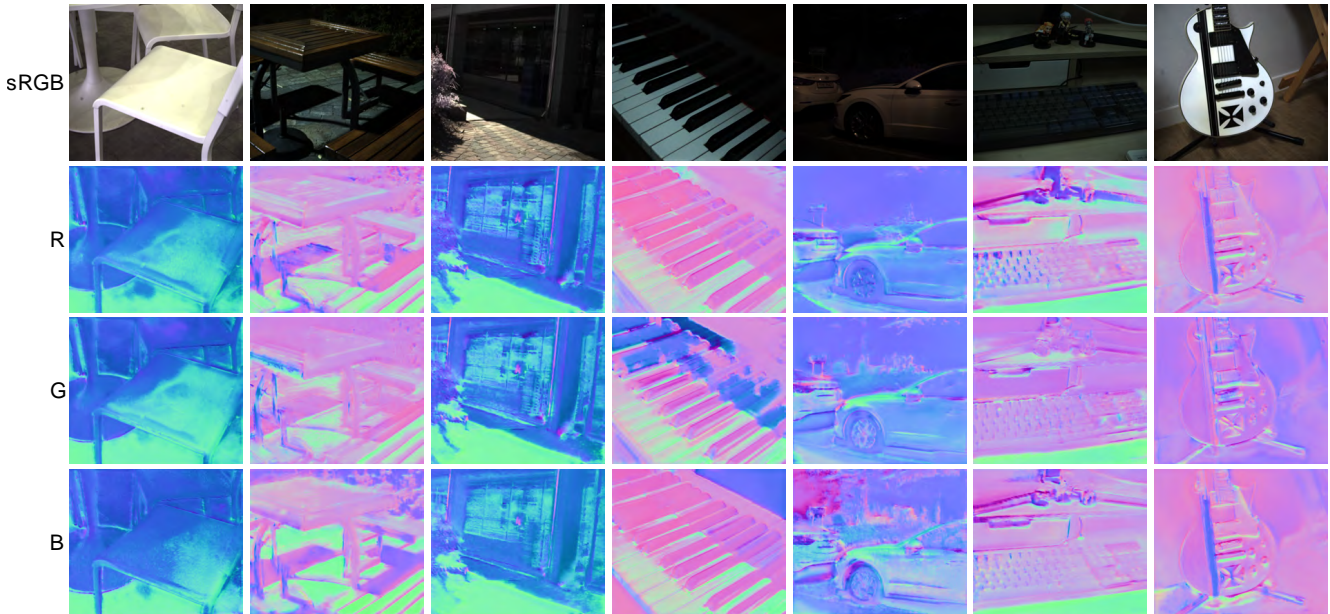
Figure 14. Additional analysis of gradient distributions with respect to dataset labels.

9. Shape from Polarization

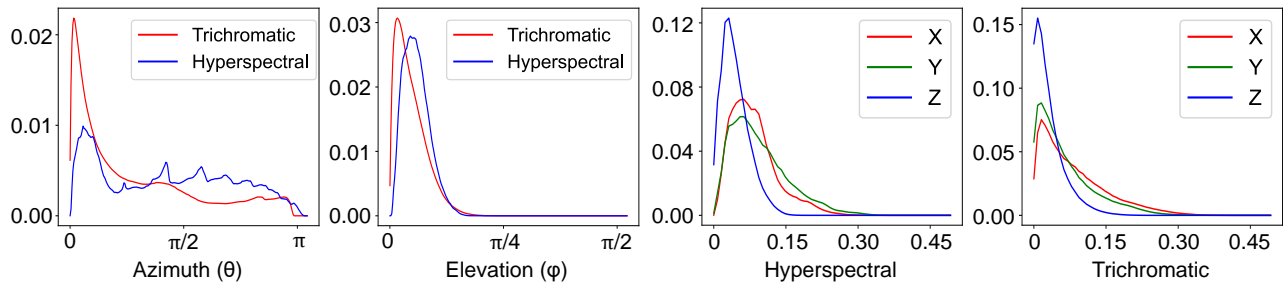
Through shape-from-polarization (SfP) methods, we can reconstruct 3D normal map from polarization data such as Stokes parameters, DoLP and AoLP information. However, as they utilize features from linear polarization state and monochromatic data, they lose consistency of normal maps along the spectral axis. Divergent normal maps recovered across different wavelengths using SfP by Lei et al. [10] from hyperspectral Stokes dataset are shown in Figure 15(a) and trichromatic Stokes dataset in Figure 15(b). In Figure 15(a), although Stokes parameters are shown to have different values for each spectrum, normal map of the scene should not be distinct, which is not accomplished by existing SfP methods. Those distinctions are observed regardless of the illumination condition and the number of spectral channels. Figure 15(b) shows various scenes from the trichromatic Stokes dataset, including sunlight, night time, white light, and yellow light. Figure 15(c) plots the standard deviation probability of azimuth θ and elevation ϕ while Figure 15(d) shows the standard deviation probability of x , y , and z components of normal maps across the spectral bands for each dataset. We can see that x and y vary more than z components leading to fluctuating azimuth, which indicates that reconstructed normal maps do not guarantee reliable x and y components. Utilizing circular polarization and hyperspectral information, SfP yields more accurate normal maps.



(a) Hyperspectral dataset



(b) Trichromatic dataset



(c) Standard deviation distribution of azimuth and elevation of normal maps

(d) Standard deviation distribution of x , y , and z components of normal maps

Figure 15. **Normal maps obtained via SfP by Lei et al. [10] and their statistics.** (a) Normal maps acquired from the same scene in hyperspectral Stokes dataset but with different wavelength. (b) Normal maps obtained from various illumination condition from the trichromatic Stokes dataset. (c) Standard deviation probability of azimuth and elevation of normal maps categorized by dataset. (d) Standard deviation probability of x , y , and z components of normal maps.

10. Dataset Examples

In this section, we present examples of our datasets in terms of sRGB, intensity and Stokes vectors (s_1 , s_2 and s_3) across the spectrum. We collected the data based on nine different labels, encompassing location and time (indoor, outdoor daytime, outdoor night), scene types (object-oriented and scene-oriented), illumination sources (white light, incandescent light, clear sunlight and cloudy conditions). Figure 16, 17 shows object-oriented scenes, characterized by one or two single objects, while Figure 18, 19 shows scene-oriented scenes. Indoor scenes are showcased in Figure 20, 21, outdoor daytime scenes in Figure 22, 23, and outdoor night scenes with low intensities in Figure 24, 25. Figure 26, 27 display data captured under white light, commonly found in indoor settings, and Figure 28, 29 shows data captured under incandescent light, known for emitting a yellowish hue. Figure 30, 31 show data captured under clear sunlight, and Figure 32, 33 display data captured under cloudy conditions. As shown in these figures, our datasets spans diverse scene types, objects times, and illumination conditions.

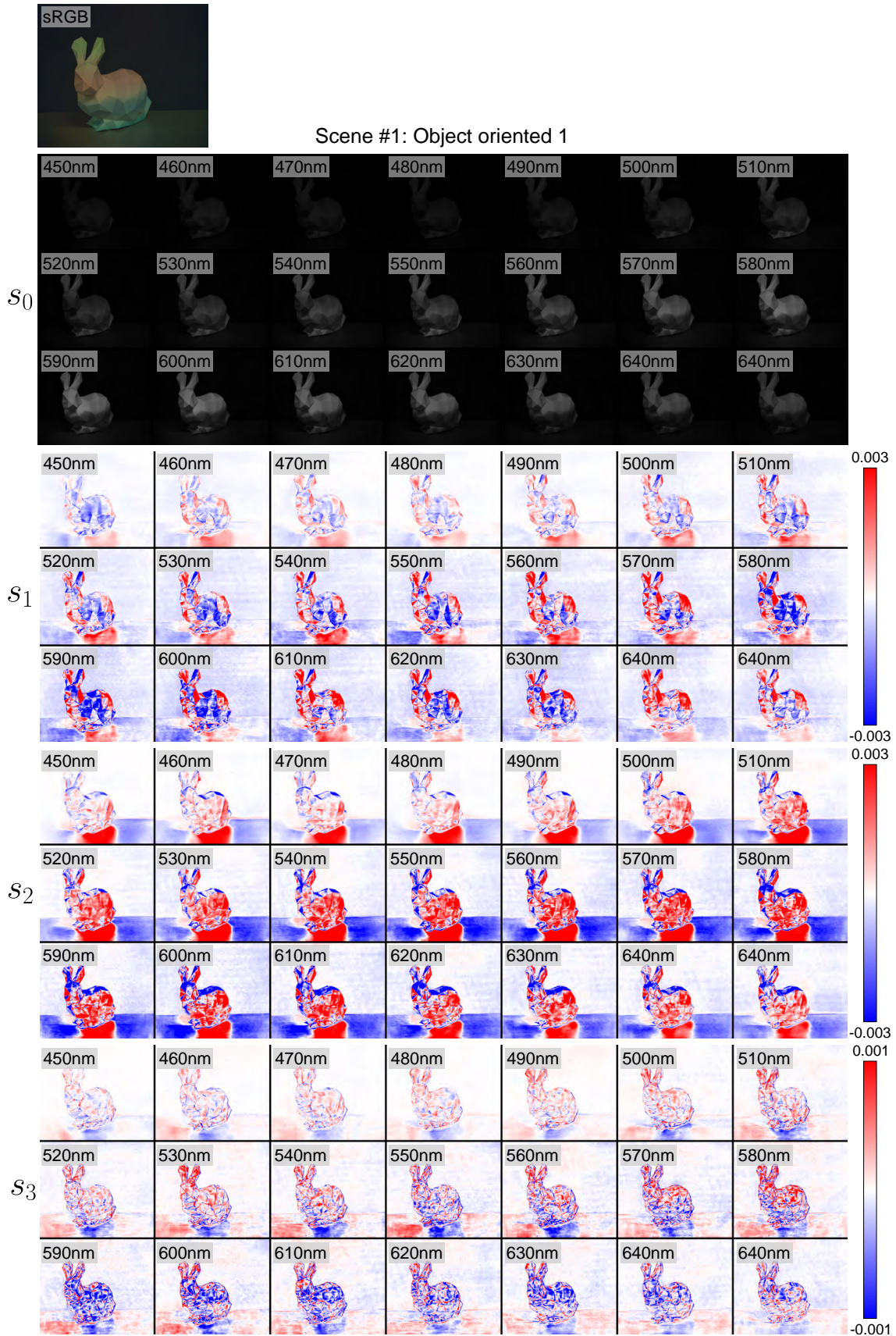


Figure 16. Dataset example of object-centric data in the hyperspectral dataset.

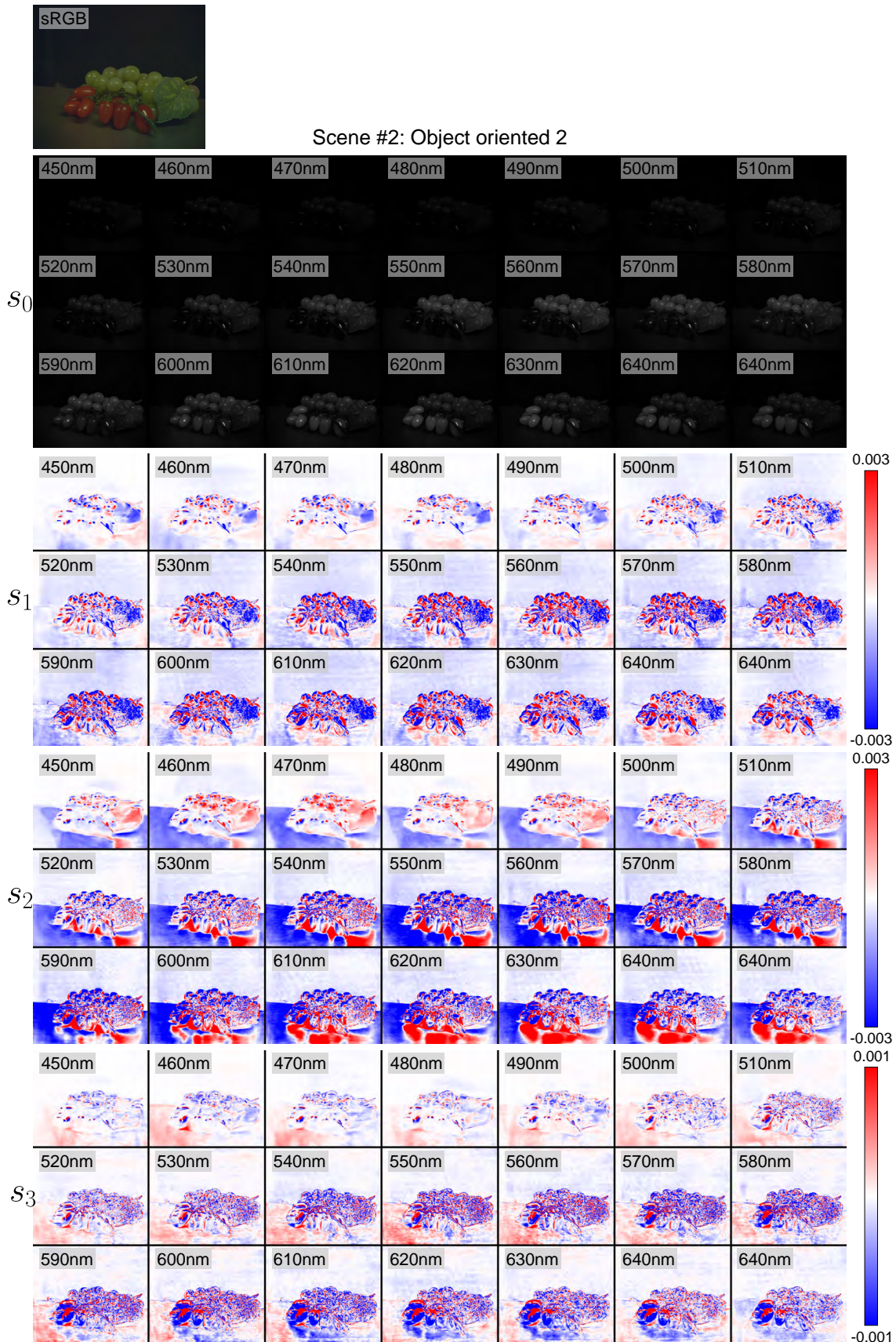


Figure 17. Dataset example of object-centric data in the hyperspectral dataset.

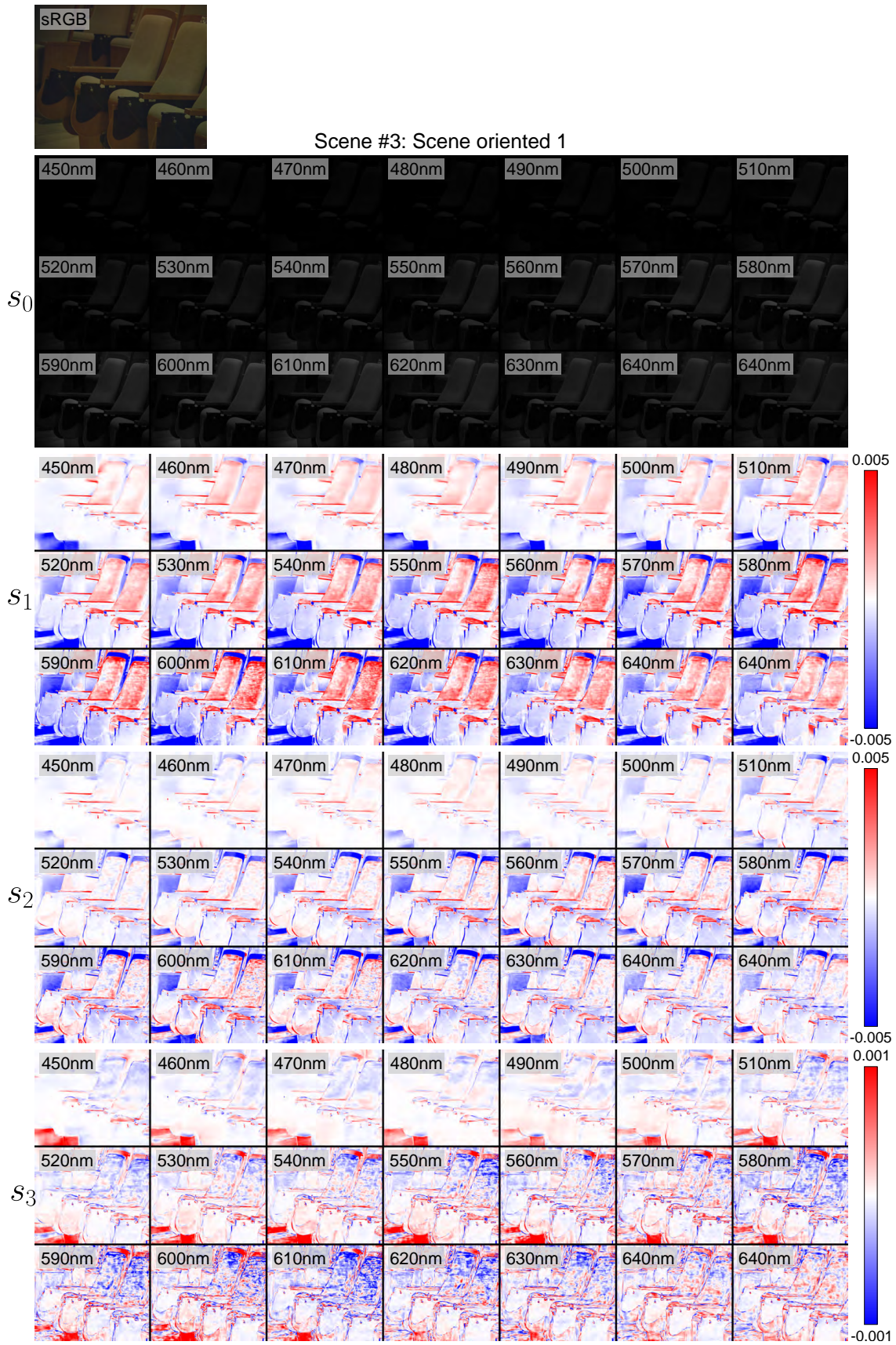


Figure 18. Dataset example of scene-centric data in the hyperspectral dataset.

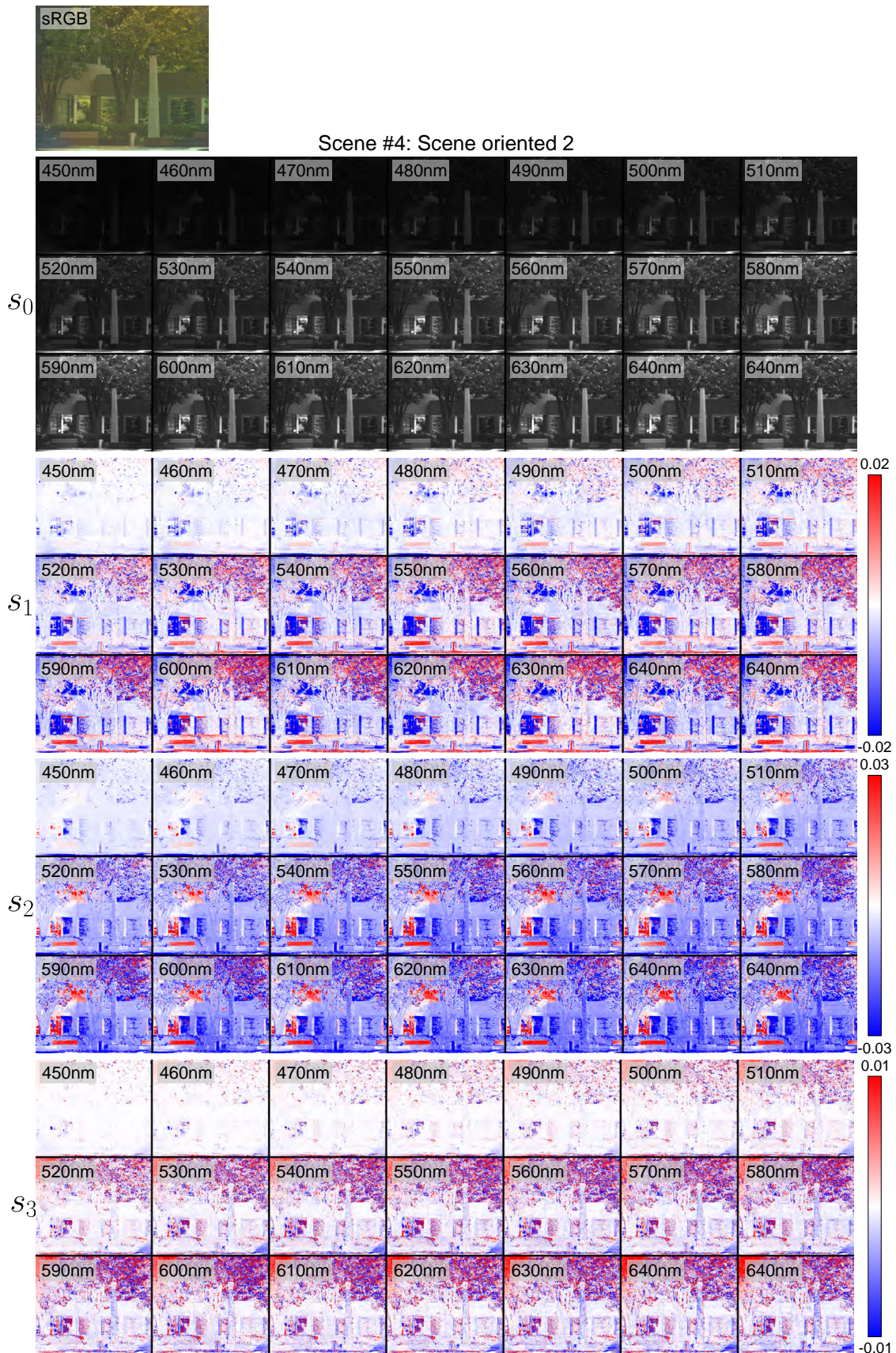


Figure 19. Dataset example of scene-centric data in the hyperspectral dataset.

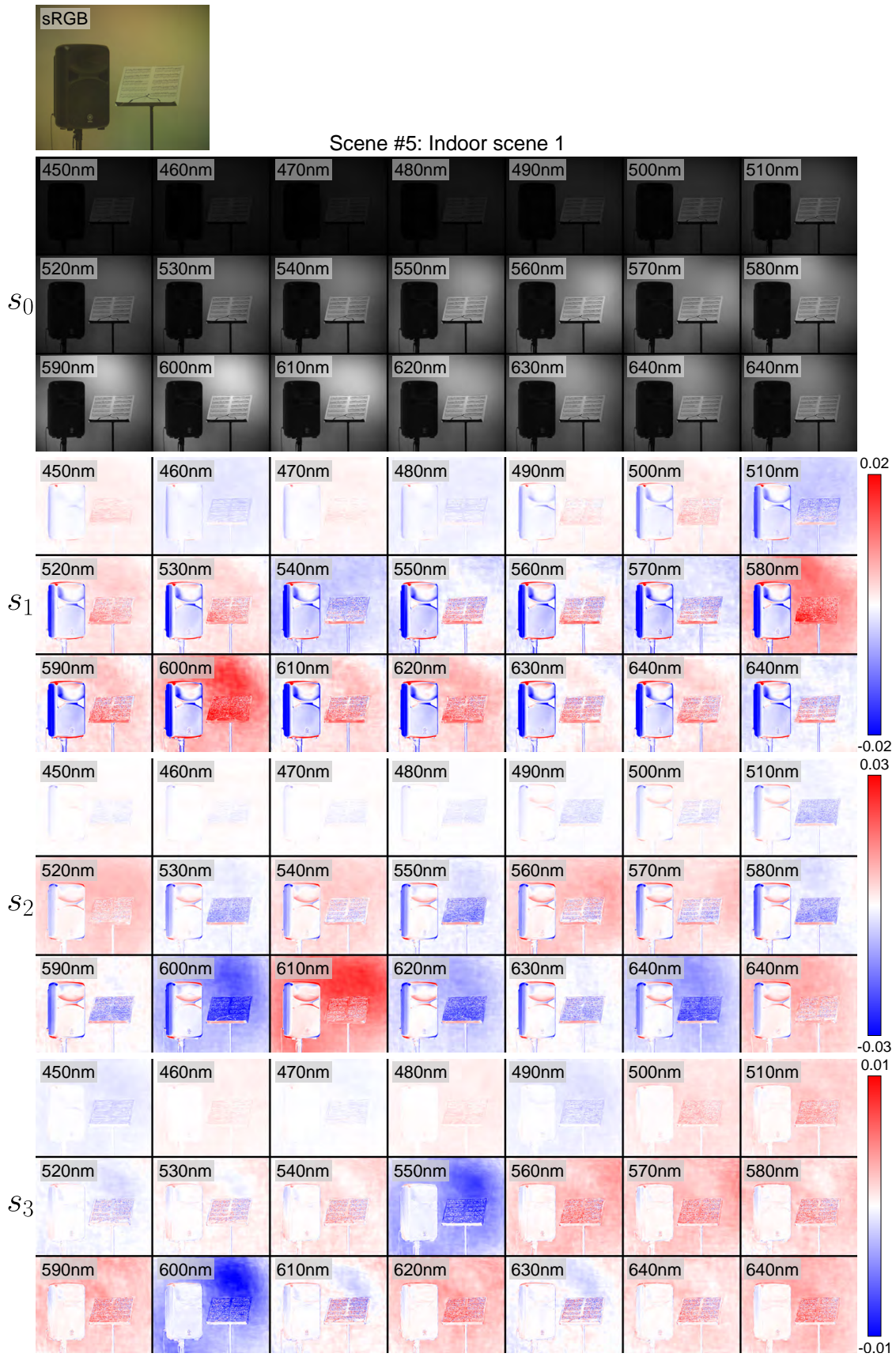


Figure 20. Dataset example of indoor scene data in the hyperspectral dataset.

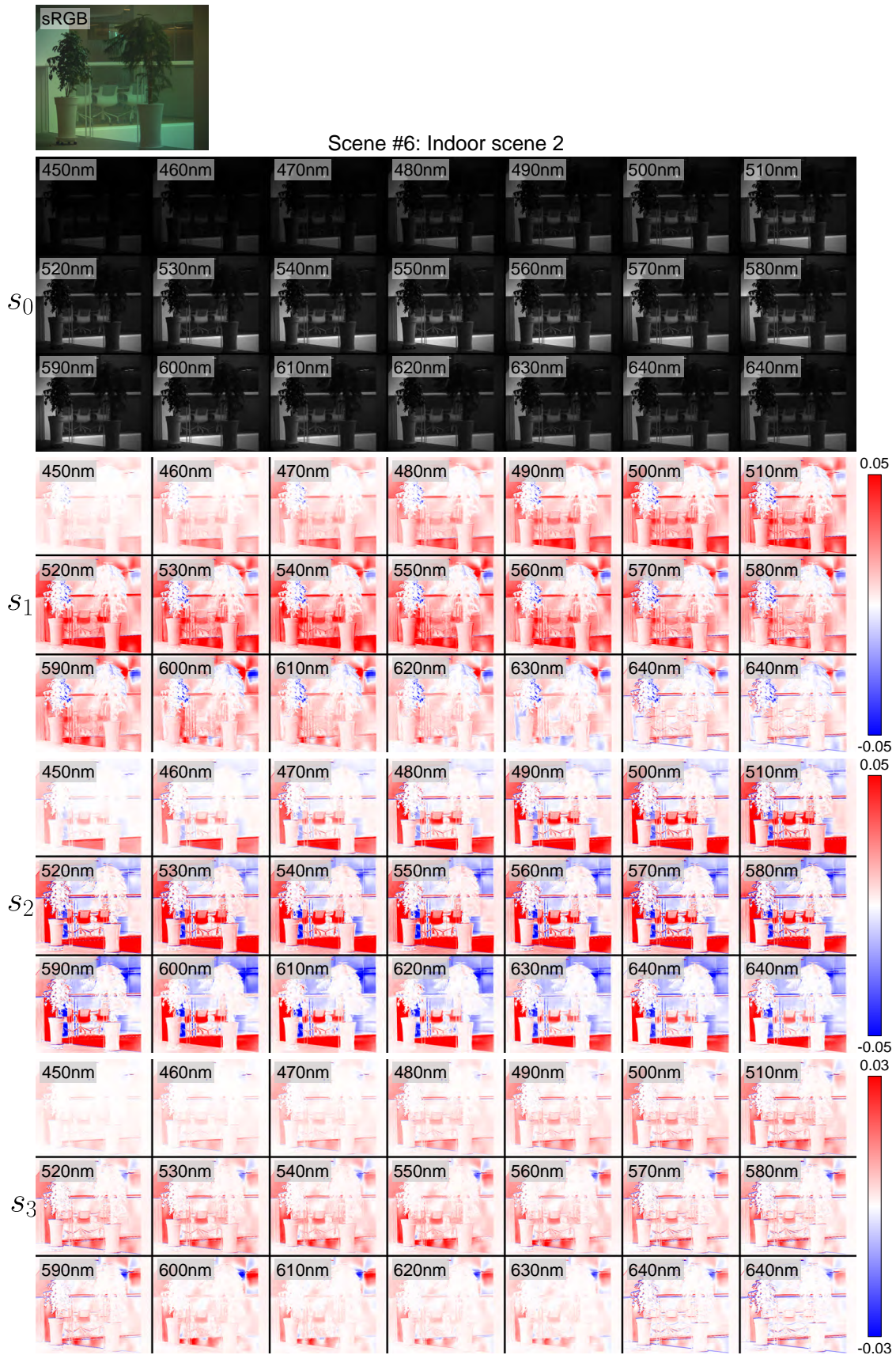


Figure 21. Dataset example of indoor scene data in the hyperspectral dataset.

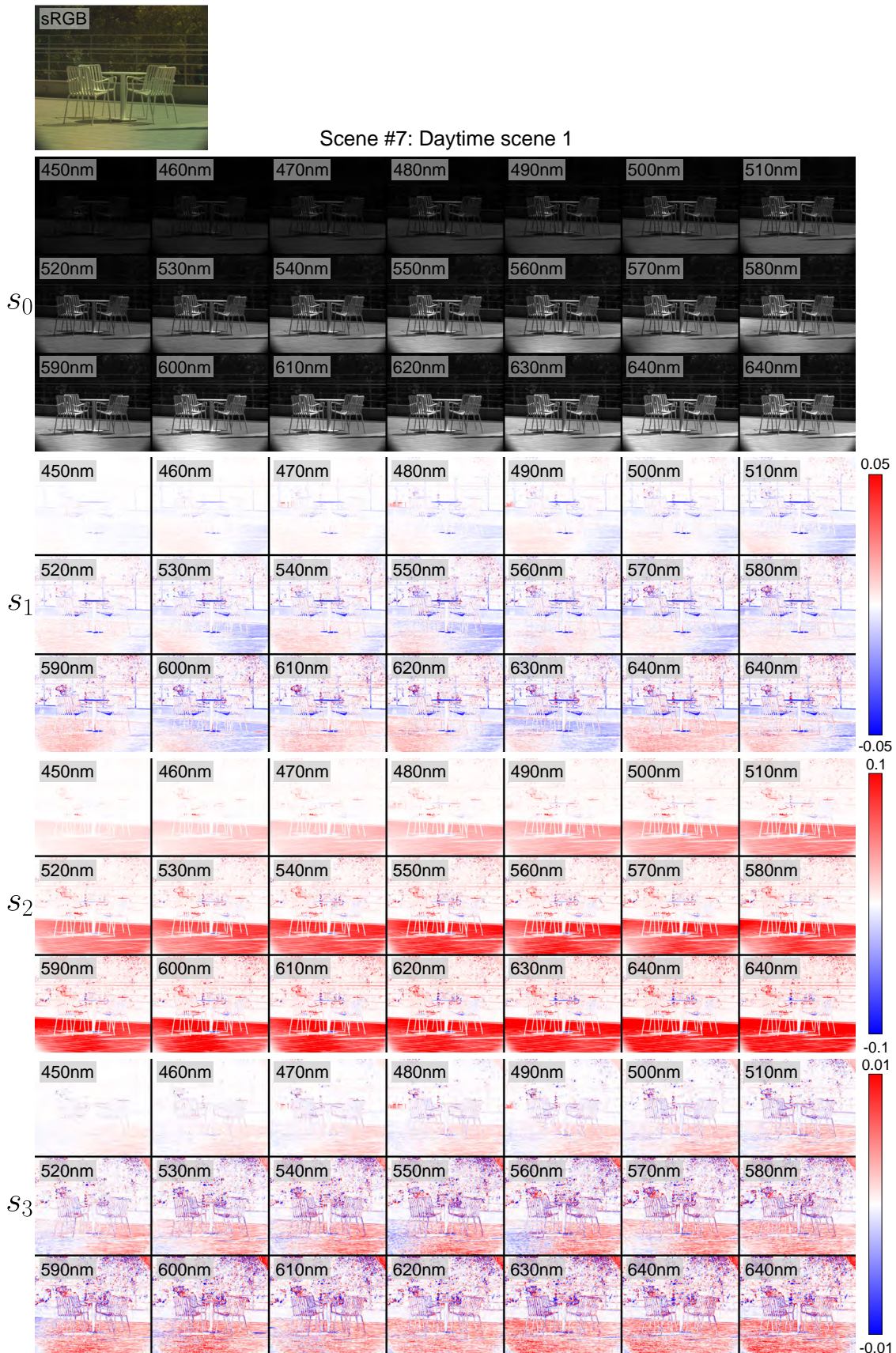


Figure 22. Dataset example of daytime scene data in the hyperspectral dataset.

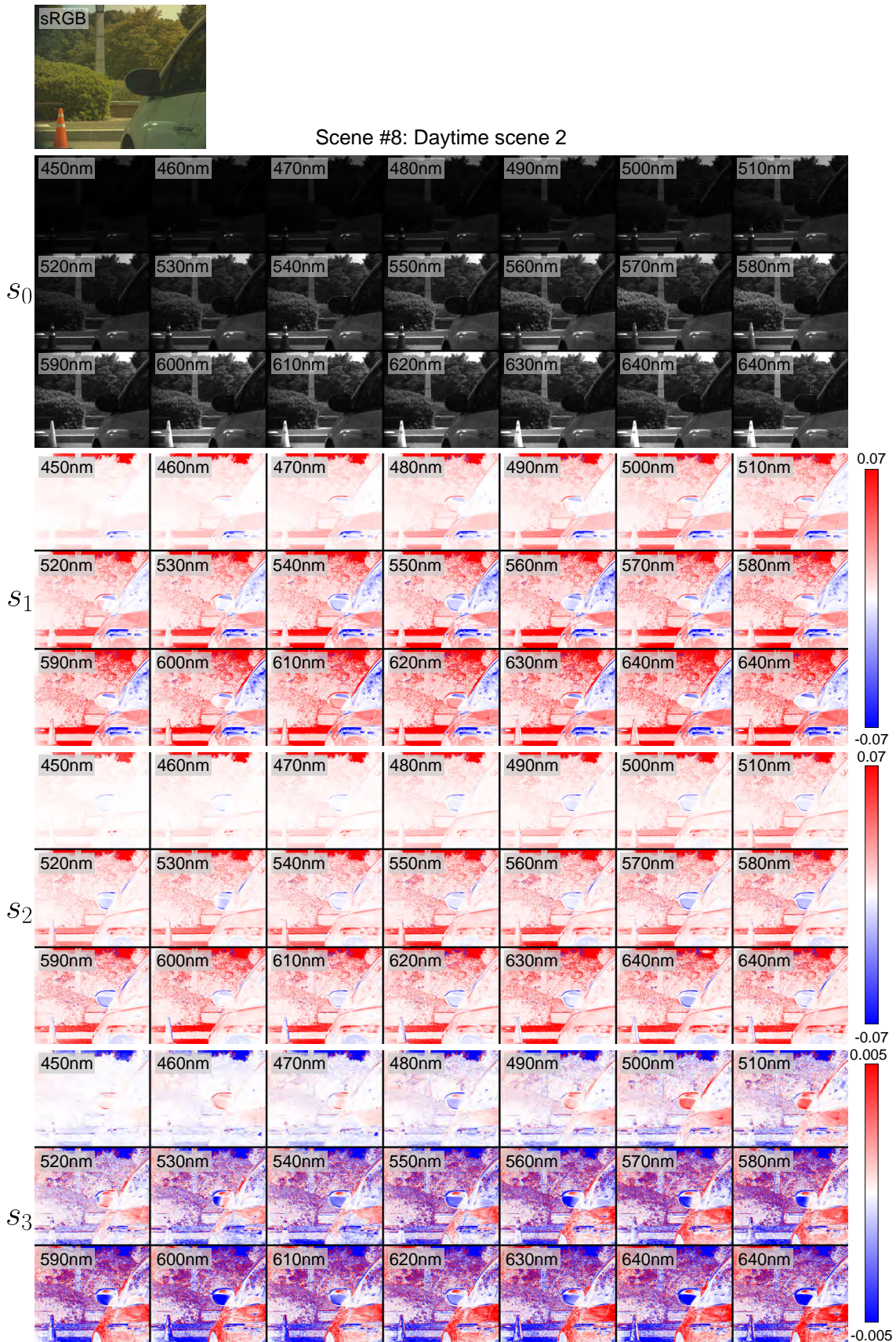


Figure 23. Dataset example of daytime scene data in the hyperspectral dataset.

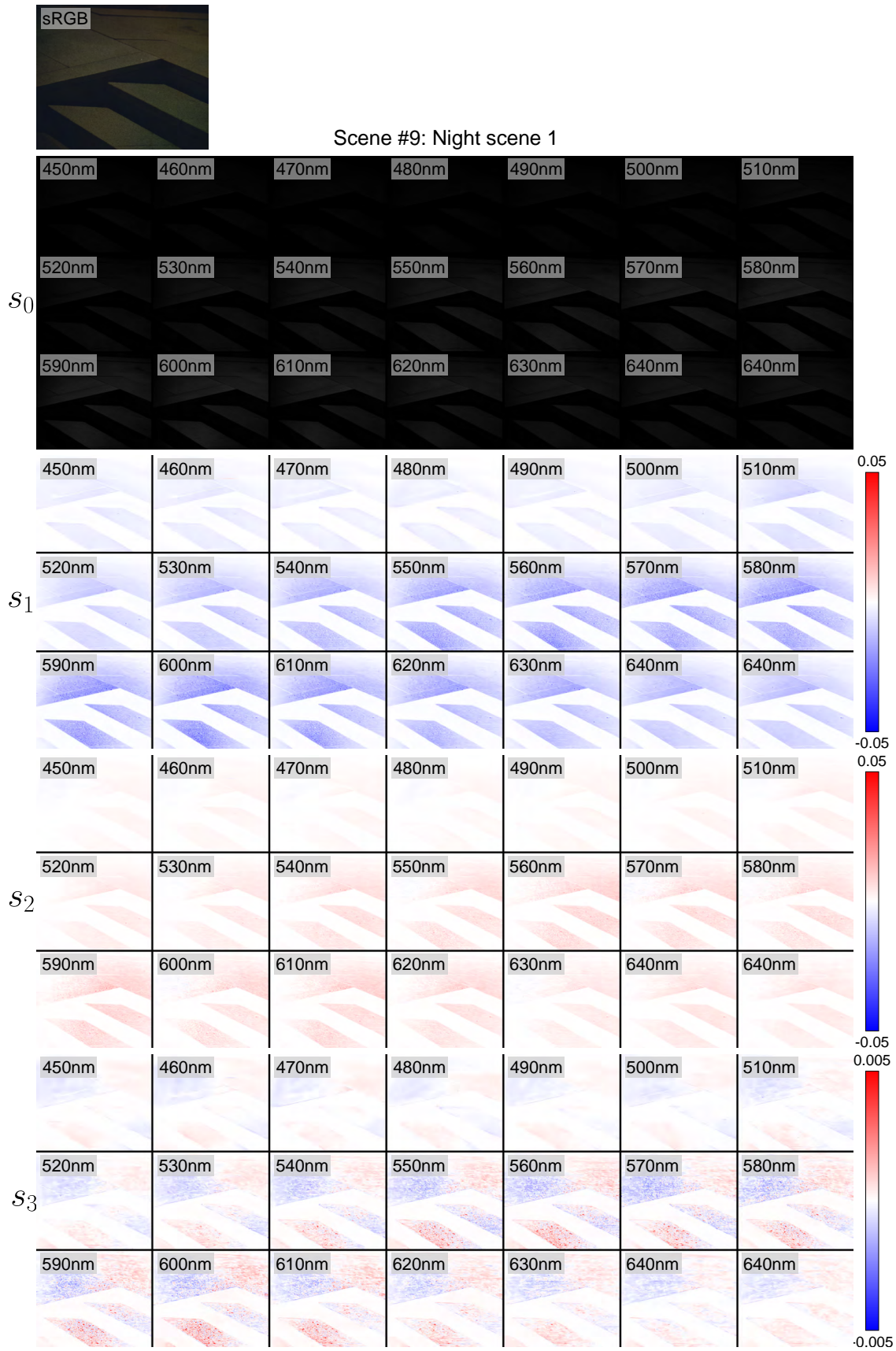


Figure 24. Dataset example of night scene data in the hyperspectral dataset.

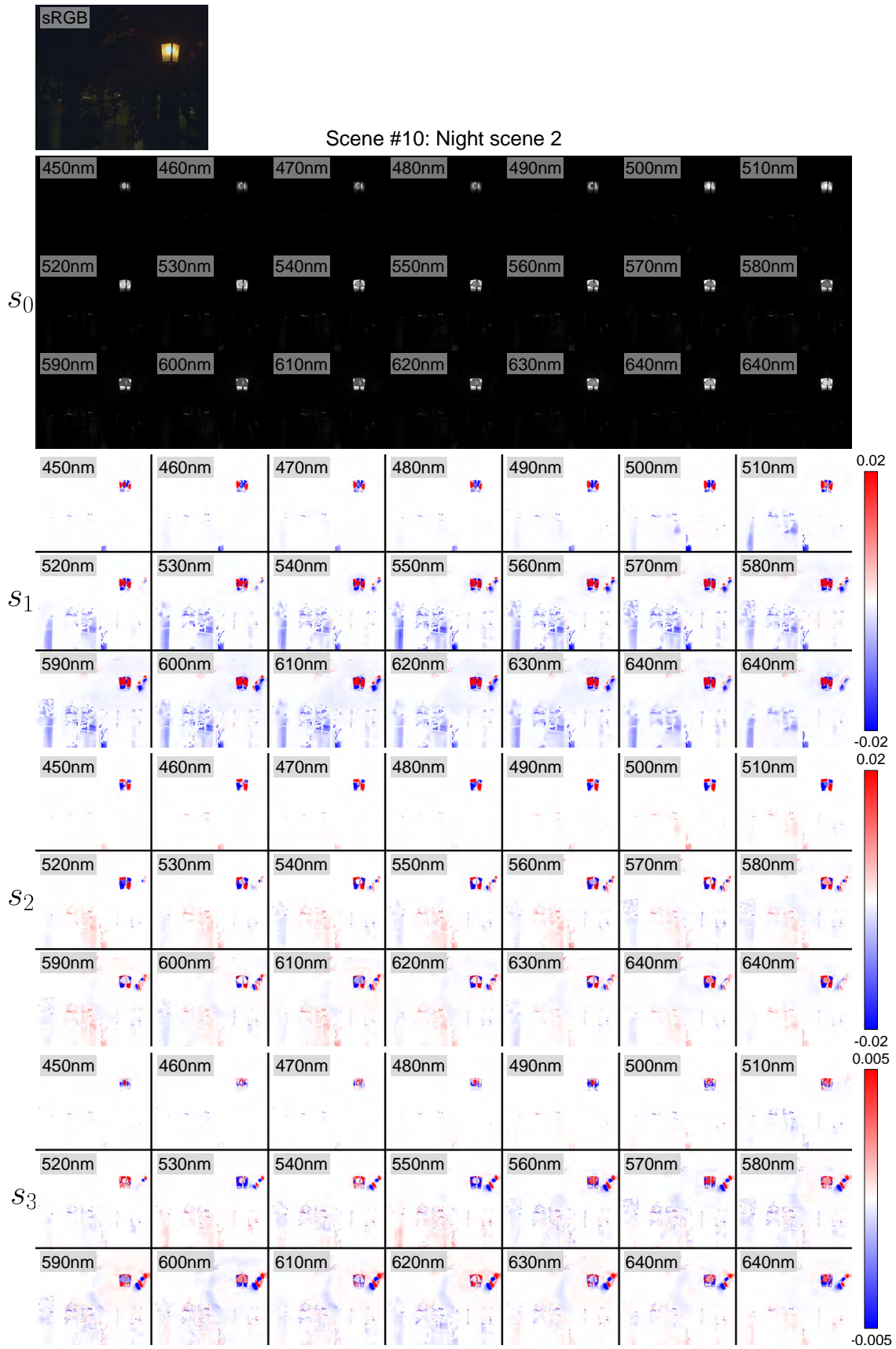


Figure 25. Dataset example of night scene data in the hyperspectral dataset.



Scene #11: White light scene 1

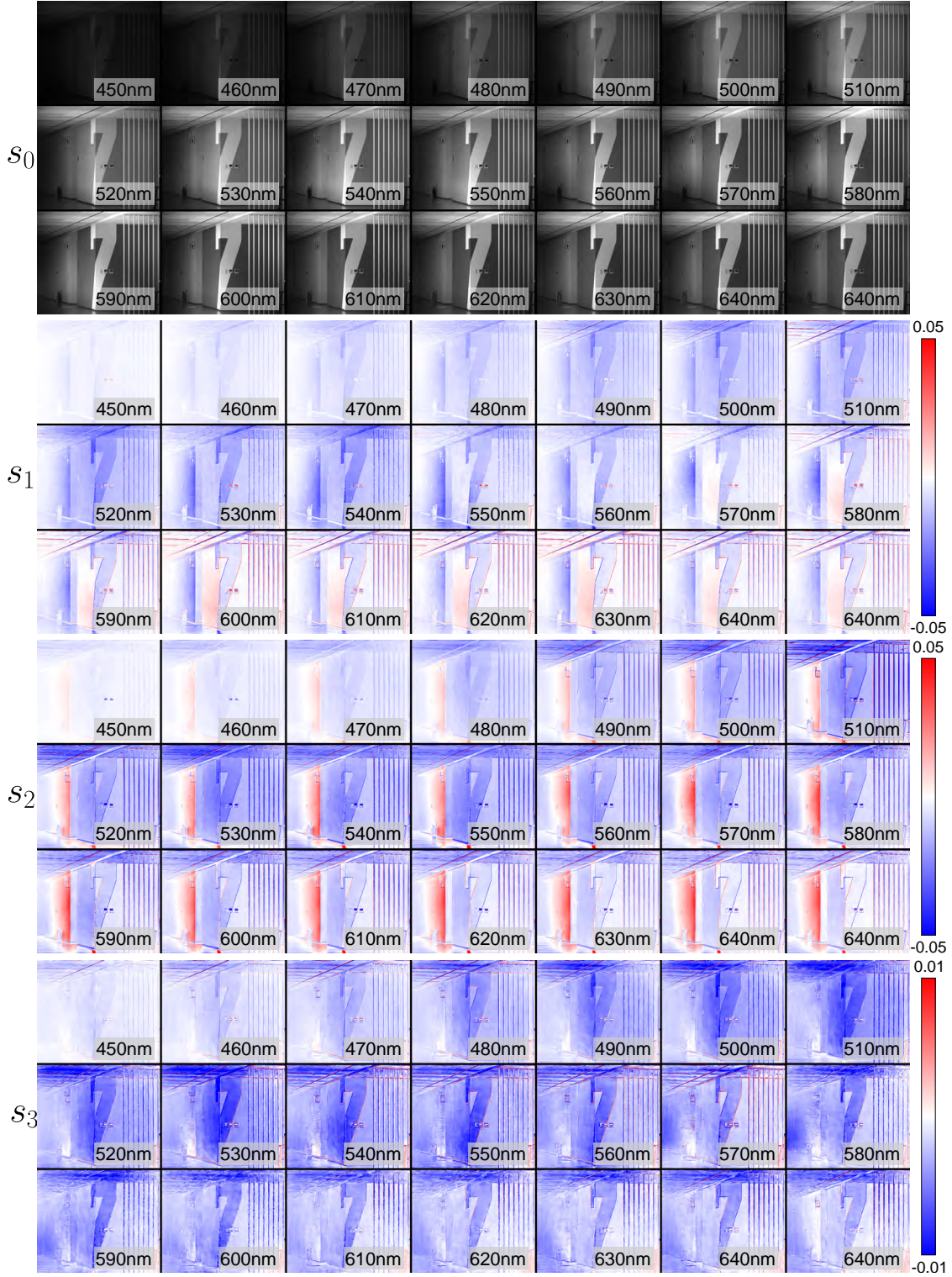


Figure 26. Dataset example of scene data captured under white light in the hyperspectral dataset.

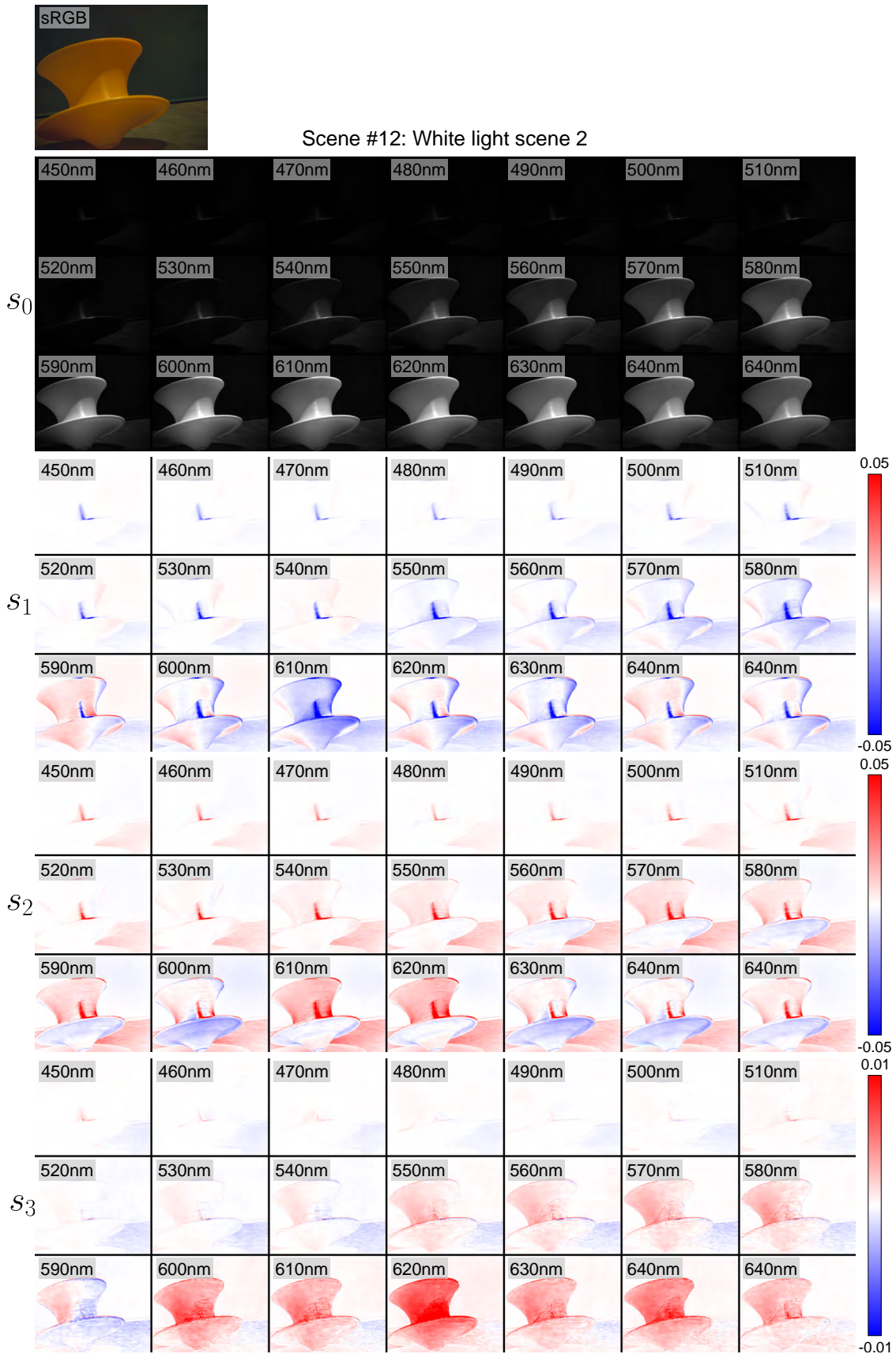


Figure 27. Dataset example of scene data captured under white light in the hyperspectral dataset.

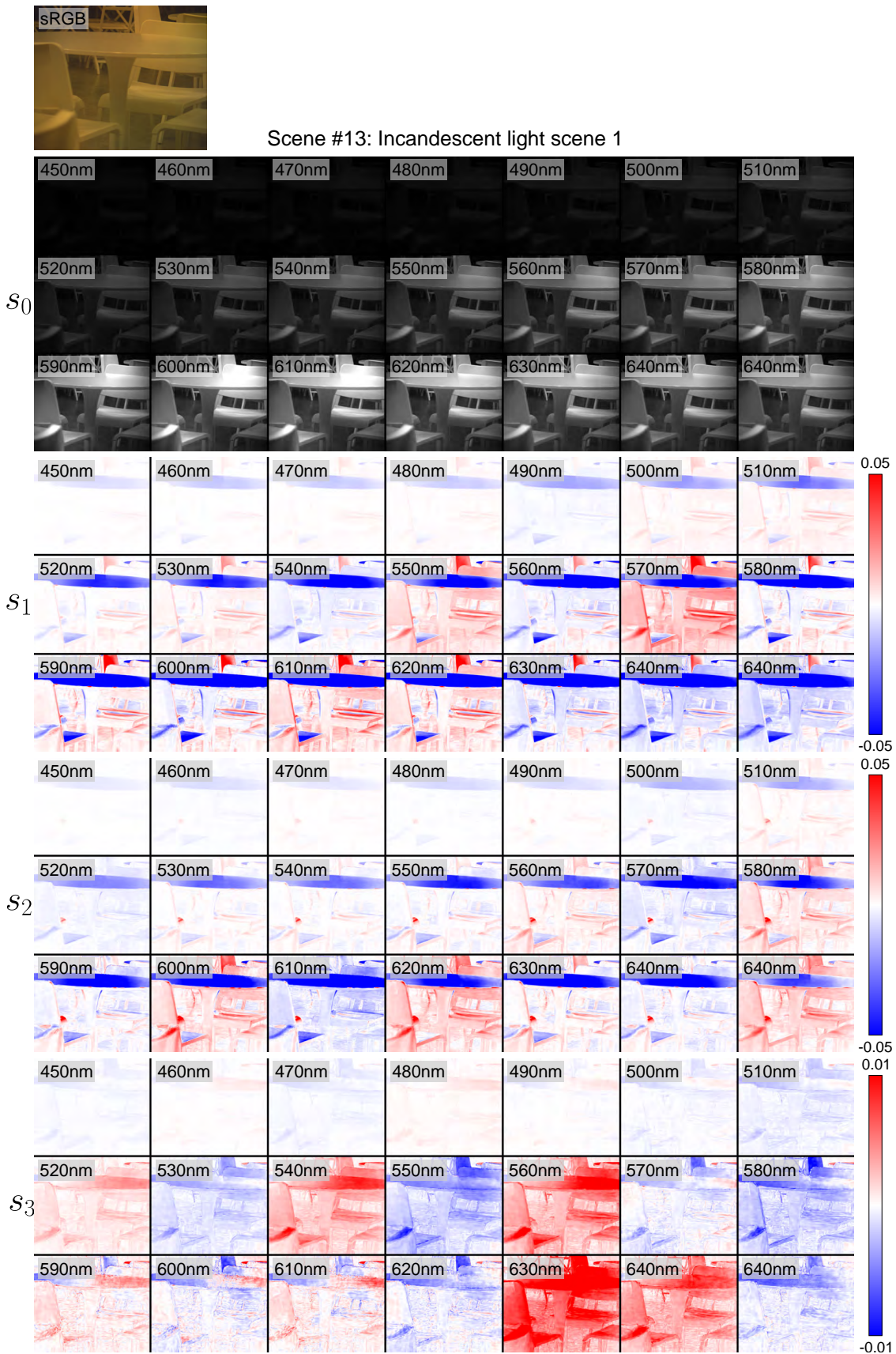


Figure 28. Dataset example of scene data captured under incandescent light in the hyperspectral dataset.

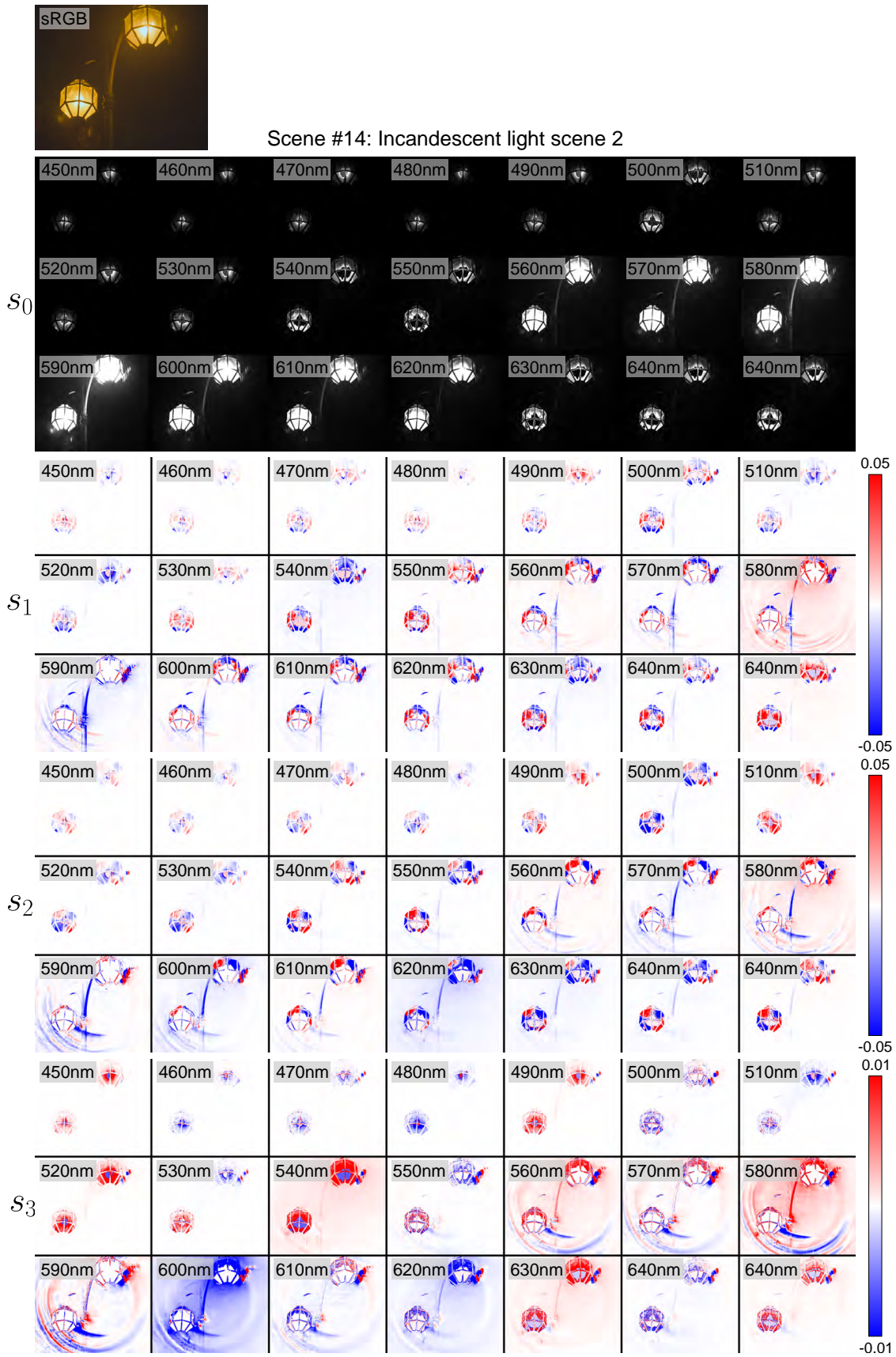


Figure 29. Dataset example of scene data captured under incandescent light in the hyperspectral dataset.



Scene #15: Sunlight scene 1

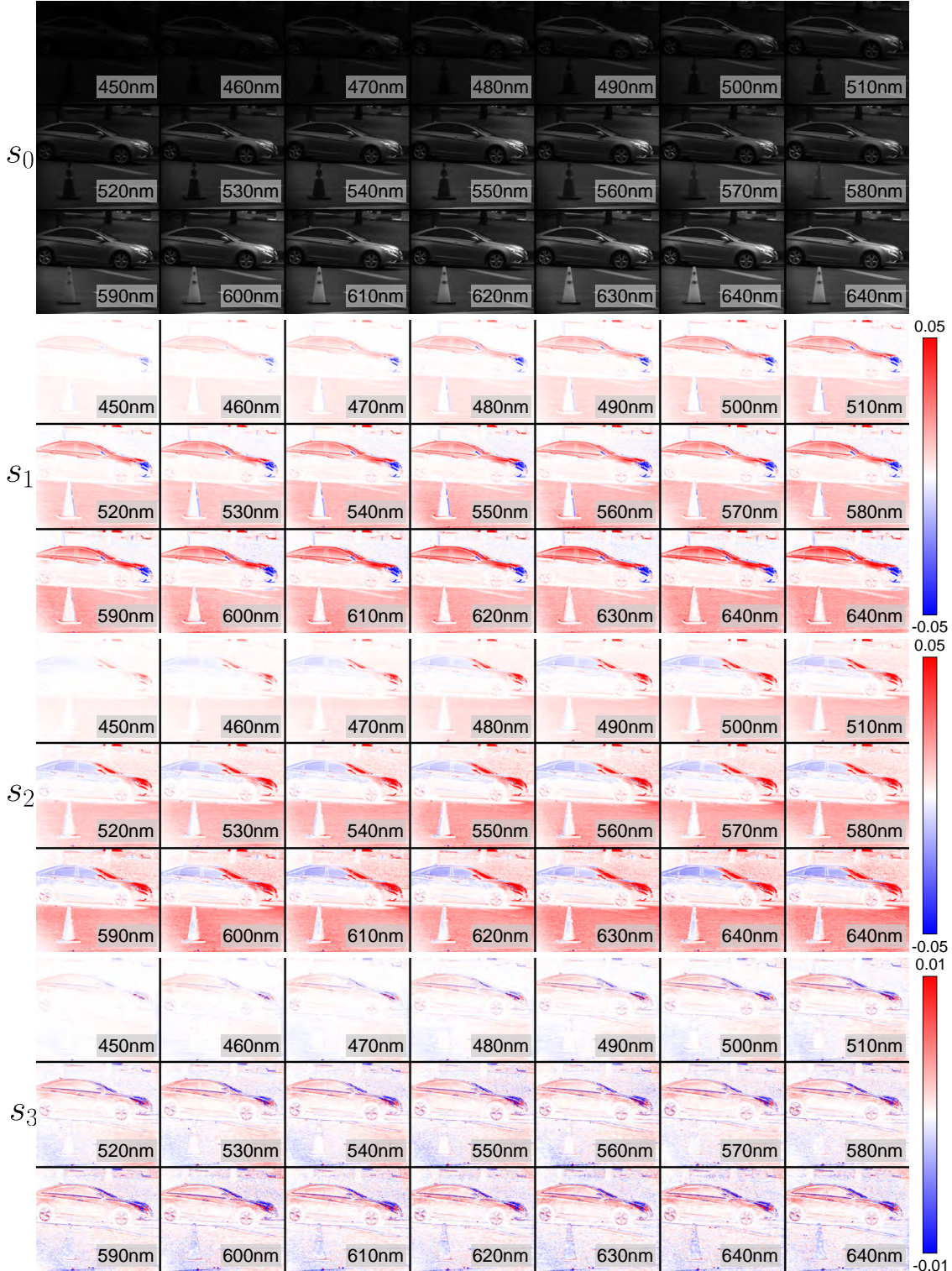


Figure 30. Dataset example of scene data captured under sunlight in the hyperspectral dataset.

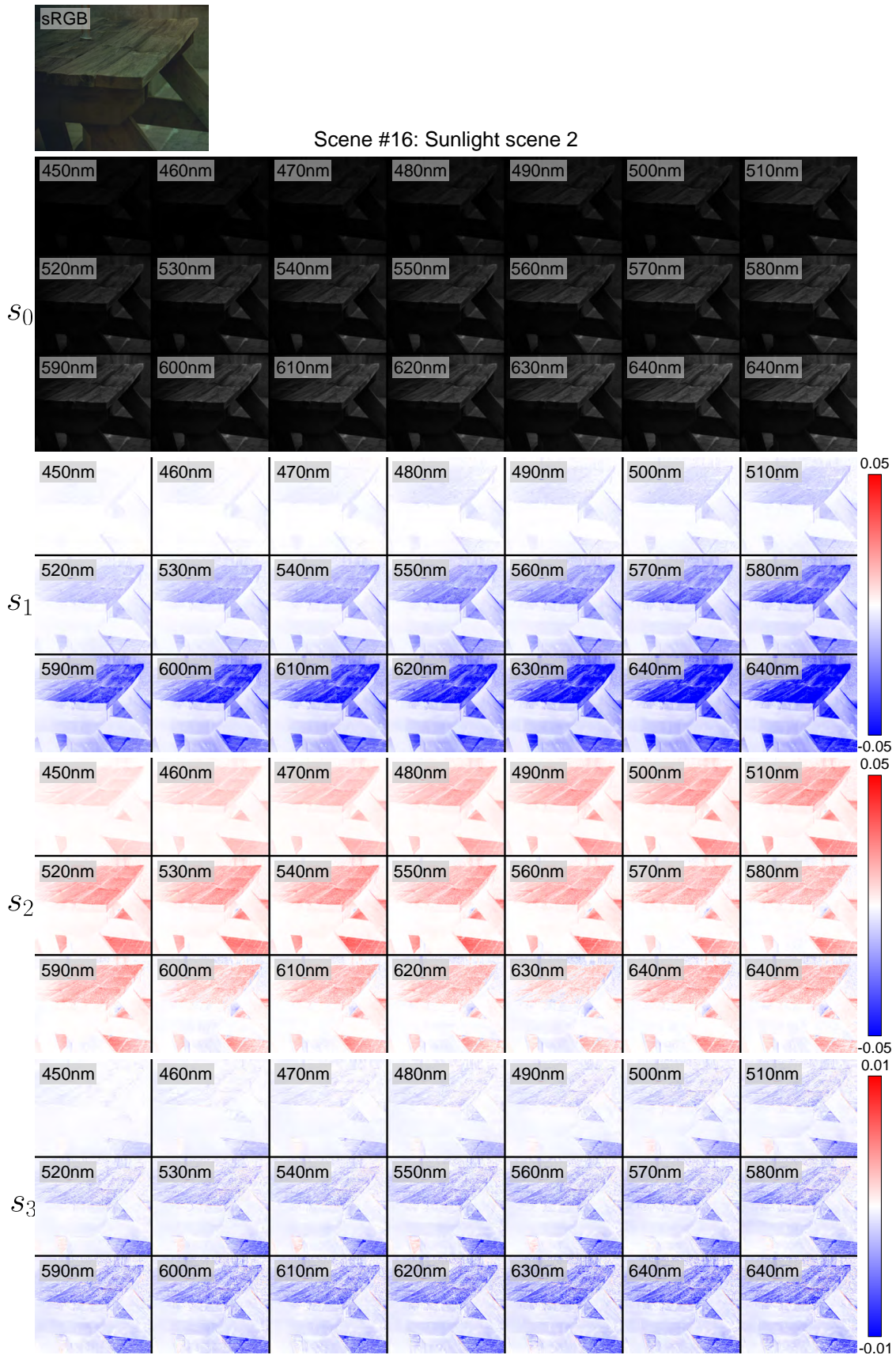


Figure 31. Dataset example of scene data captured under sunlight in the hyperspectral dataset.

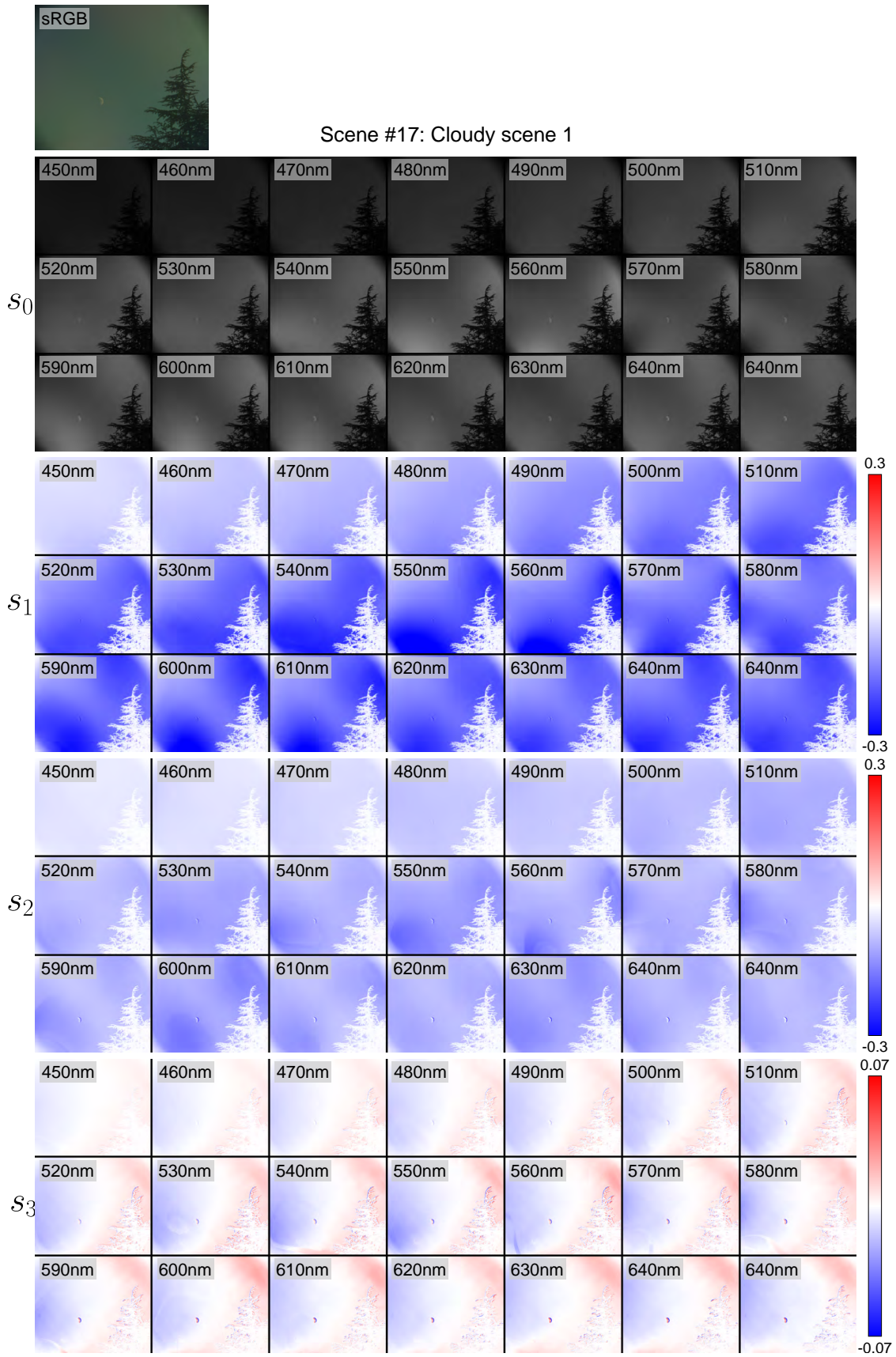


Figure 32. Dataset example of scene data captured under cloudy condition in the hyperspectral dataset.



Scene #18: Cloudy scene 2

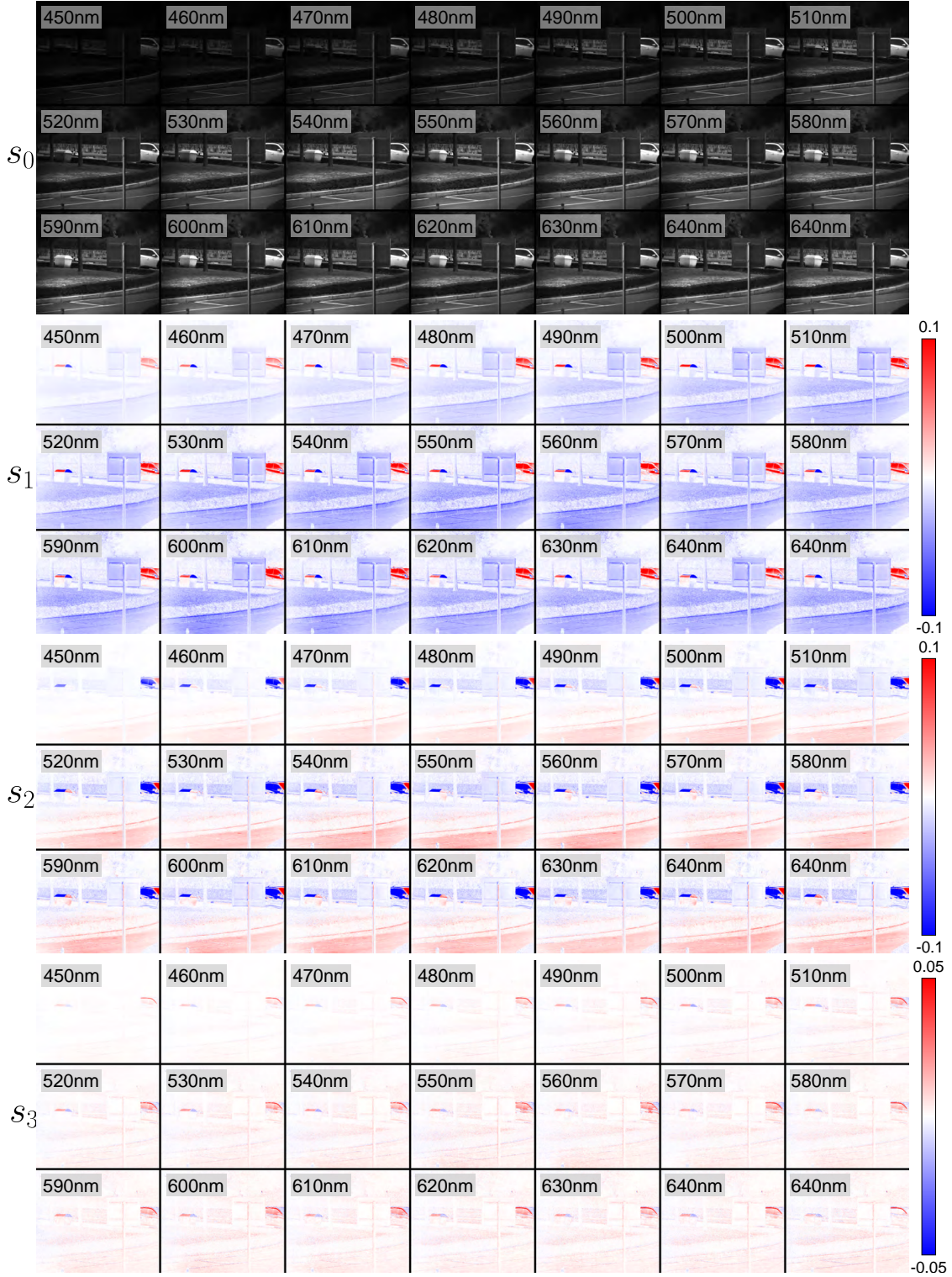


Figure 33. Dataset example of scene data captured under cloudy condition in the hyperspectral dataset.

References

- [1] Yunhao Ba, Alex Gilbert, Franklin Wang, Jinfa Yang, Rui Chen, Yiqin Wang, Lei Yan, Boxin Shi, and Achuta Kadambi. Deep shape from polarization. In *Eur. Conf. Comput. Vis.*, pages 554–571. Springer, 2020. 2
- [2] Akshat Dave, Yongyi Zhao, and Ashok Veeraraghavan. Pandora: Polarization-aided neural decomposition of radiance. *arXiv preprint arXiv:2203.13458*, 2022. 2
- [3] Axin Fan, Tingfa Xu, Geer Teng, Wang Xi, Yuhan Zhang, Chang Xu, Xin Xu, and Jianan Li. Full-stokes polarization multispectral images of various stereoscopic objects. *Scientific Data*, 10, 05 2023. 2
- [4] Daoyi Gao, Yitong Li, Patrick Ruhkamp, Iuliia Skobleva, Magdalena Wysocki, HyunJun Jung, Pengyuan Wang, Arturo Guridi, and Benjamin Busam. Polarimetric pose prediction. In *Eur. Conf. Comput. Vis.*, October 2022. 2
- [5] Youngchan Kim, Wonjoon Jin, Sunghyun Cho, and Seung-Hwan Baek. Neural spectro-polarimetric fields. *arXiv preprint arXiv:2306.12562*, 2023. 2, 3, 6
- [6] Yuhi Kondo, Taishi Ono, Legong Sun, Yasutaka Hirasawa, and Jun Murayama. Accurate polarimetric brdf for real polarization scene rendering. In *Eur. Conf. Comput. Vis.*, pages 220–236. Springer, 2020. 2
- [7] Teppei Kurita, Yuhi Kondo, Legong Sun, and Yusuke Moriuchi. Simultaneous acquisition of high quality rgb image and polarization. In *Proceedings of the IEEE/CVF Winter Conference on Applications of Computer Vision (WACV)*, pages 178–188, January 2023. 2
- [8] Pierre-Jean Lapray, Luc Gendre, Alban Foulonneau, and Laurent Bigué. Database of polarimetric and multispectral images in the visible and nir regions. 04 2018. 2
- [9] Chenyang Lei, Xuhua Huang, Mengdi Zhang, Qiong Yan, Wenxiu Sun, and Qifeng Chen. Polarized reflection removal with perfect alignment in the wild. In *IEEE Conf. Comput. Vis. Pattern Recog.*, June 2020. 2
- [10] Chenyang Lei, Chenyang Qi, Jiabin Xie, Na Fan, Vladlen Koltun, and Qifeng Chen. Shape from polarization for complex scenes in the wild. In *IEEE Conf. Comput. Vis. Pattern Recog.*, pages 12632–12641, June 2022. 2, 20, 21
- [11] Yupeng Liang, Ryosuke Wakaki, Shohei Nobuhara, and Ko Nishino. Multimodal material segmentation. In *IEEE Conf. Comput. Vis. Pattern Recog.*, pages 19800–19808, June 2022. 2
- [12] Youwei Lyu, Zhaopeng Cui, Si Li, Marc Pollefeys, and Boxin Shi. Reflection separation using a pair of unpolarized and polarized images. In H. Wallach, H. Larochelle, A. Beygelzimer, F. d'Alché-Buc, E. Fox, and R. Garnett, editors, *Adv. Neural Inform. Process. Syst.*, volume 32. Curran Associates, Inc., 2019. 2
- [13] Haiyang Mei, Bo Dong, Wen Dong, Jiayi Yang, Seung-Hwan Baek, Felix Heide, Pieter Peers, Xiaopeng Wei, and Xin Yang. Glass segmentation using intensity and spectral polarization cues. In *IEEE Conf. Comput. Vis. Pattern Recog.*, pages 12622–12631, 2022. 2
- [14] Simeng Qiu, Qiang Fu, Congli Wang, and Wolfgang Heidrich. Linear polarization demosaicking for monochrome and colour polarization focal plane arrays. *Comput. Graph. Forum*, 40, 03 2021. 2
- [15] Matthew Tancik, Pratul P. Srinivasan, Ben Mildenhall, Sara Fridovich-Keil, Nithin Raghavan, Utkarsh Singhal, Ravi Ramamoorthi, Jonathan T. Barron, and Ren Ng. Fourier features let networks learn high frequency functions in low dimensional domains. *NeurIPS*, 2020. 6
- [16] Xingzhou Tu, Oliver J Spires, Xiaobo Tian, Neal Brock, Rongguang Liang, and Stanley Pau. Division of amplitude rgb full-stokes camera using micro-polarizer arrays. *Optics Express*, 25(26):33160–33175, 2017. 3
- [17] Yi Zhang, Dasong Li, Xiaoyu Shi, Dailan He, Kangning Song, Xiaogang Wang, Hongwei Qin, and Hongsheng Li. Kbnnet: Kernel basis network for image restoration, 2023. 4, 5, 8